

Key Points:

- Temporal and spatial variations of semidiurnal internal tides are observed using in situ moorings and satellite altimetry
- Complex internal tide field is caused by multiple generation sources, seasonal stratification, and likely mesoscale eddies
- The three generation sources of mode-1 M_2 internal tides are subject to strong but different seasonalities

Supporting Information:

Supporting Information may be found in the online version of this article.

Correspondence to:

T. Cai,
joycecai@uw.edu

Citation:

Cai, T., Zhao, Z., D'Asaro, E., Wang, J., & Fu, L.-L. (2024). Internal tide variability off Central California: Multiple sources, seasonality, and eddying background.

Journal of Geophysical Research: Oceans, 129, e2024JC020892. <https://doi.org/10.1029/2024JC020892>

Received 7 JAN 2024

Accepted 26 JUL 2024

Author Contributions:

Conceptualization: Zhongxiang Zhao, Jinbo Wang

Data curation: Tongxin Cai

Formal analysis: Tongxin Cai, Zhongxiang Zhao, Eric D'Asaro

Funding acquisition: Zhongxiang Zhao

Methodology: Tongxin Cai, Zhongxiang Zhao, Eric D'Asaro, Jinbo Wang, Lee-Lueng Fu

Project administration:

Zhongxiang Zhao

Supervision: Zhongxiang Zhao

Validation: Tongxin Cai

Visualization: Tongxin Cai

Writing – original draft: Tongxin Cai, Zhongxiang Zhao, Eric D'Asaro, Jinbo Wang, Lee-Lueng Fu

Writing – review & editing: Tongxin Cai, Zhongxiang Zhao, Eric D'Asaro, Jinbo Wang, Lee-Lueng Fu

Internal Tide Variability Off Central California: Multiple Sources, Seasonality, and Eddying Background

Tongxin Cai^{1,2} , Zhongxiang Zhao^{1,2} , Eric D'Asaro^{1,2} , Jinbo Wang³ , and Lee-Lueng Fu³ 

¹Applied Physics Laboratory, University of Washington, Seattle, WA, USA, ²School of Oceanography, University of Washington, Seattle, WA, USA, ³Jet Propulsion Laboratory, California Institute of Technology, Pasadena, CA, USA

Abstract Two moorings deployed for 75 days in 2019 and long-term satellite altimetry data reveal a spatially complex and temporally variable internal tidal field at the Surface Water and Ocean Topography (SWOT) Cal/Val site off central California due to the interference of multiple seasonally-variable sources. These two data sets offer complementary insights into the variability of internal tides in various time scales. The in situ measurements capture variations occurring from days to months, revealing ~45% coherent tides. The north mooring displays stronger mode-1 M_2 with an amplitude of ~5.1 mm and exhibits distinct time-varying energy and modal partitioning compared to the south mooring, which is only 30-km away. The 27-year altimetry data unveils the mean and seasonal variations of internal tides. The results indicate that the complex internal tidal field is attributed to multiple sources and seasonality. Mode-1 tides primarily originate from the Mendocino Ridge and the 36.5–37.5°N California continental slope, while mode-2 tides are generated by local seamounts and Monterey Bay. Seasonality is evident for mode-1 waves from three directions. The highest variability of energy flux is found in the westward waves (±22%), while the lowest is in the southward waves (±13%). The large variability observed from the moorings cannot be solely explained by seasonality; additional factors like mesoscale eddies also play a role. This study emphasizes the importance of incorporating the seasonality and spatial variability of internal tides for the SWOT internal tidal correction, particularly in regions characterized by multiple tidal sources.

Plain Language Summary This study explores the variations of internal tides, which are waves at tidal frequencies beneath the ocean surface. They play a crucial role in deep-ocean mixing, ocean circulation, and the overall climate system by transporting nutrients, heat, and carbon within the ocean. Our research area is off central California. We use both in situ measurement and satellite observation to understand how internal tides change over time and space. Our discoveries suggest that four main sources, changing ocean currents, and seasonal variations of internal tides, contribute to these tidal changes and create the complicated tidal field off central California.

1. Introduction

Investigating the internal tidal field off the U.S. west coast is like peeling an onion. Despite years of collaborative efforts within the research community, there are still many layers to uncover due to its complexity. The complexity, which manifests as temporal and spatial variations, is mainly related to the origins, pathways, and dissipation of internal tides. Previous observations and numerical simulations have identified the Mendocino Ridge (Alford, 2010), continental slope (Buijsman et al., 2012; Carter et al., 2005), local seamounts (Brink, 1995), and the Hawaiian Ridge (Zhao, 2019), as the main sources of these internal tides. After being generated, internal tides in the California Current System (CCS) are subject to the modulation of time-varying mesoscale eddies and background currents (Kurian et al., 2011), leading to temporal variations across various time scales. These combined influences contribute to the intricate nature of the internal tidal field off the U.S. west coast. Research on internal tides holds significance for biological production and climate change because the fluctuations of heat, energy, nutrients, and other climatically significant tracers, such as carbon and greenhouse gases, within the ocean interior are influenced by internal tides and the resulting vertical mixing (Melet et al., 2022; Sharples et al., 2007). Here, we analyze the spatial and temporal variations of internal tides off central California using both 75-day moored data and 27-year satellite altimetry observation.

There are four dominant sources of internal tides off the U.S. west coast. First, the Mendocino Ridge contributes strong internal tides, primarily the M_2 constituent (Alford, 2010; Althaus et al., 2003), which subsequently

propagate in a north-south direction (Zhao et al., 2019). Second, internal tides have been identified along the continental slope off Washington State (Alford et al., 2012), Oregon State (Torgrimson & Hickey, 1979), and California State. In California, Monterey Bay (Carter et al., 2005; Terker et al., 2014; Zhao et al., 2012) and the South California Bight (Buijsman et al., 2012; Johnston & Rudnick, 2015) have been focal points of research from both observational and numerical perspectives. Additionally, local seamounts, such as Fieberling Tablemount (32.5°N, 127.7°W) and Hoke Seamount (32.1°N, 126.9°W), play a role in internal tide generation (Kunze & Toole, 1997; Zhao, 2018). More recently, satellite altimetry data (Zhao, 2019) have provided evidence of another source of internal tides, demonstrating that far-field internal tides originate remotely from the Hawaiian Ridge. The significance of these remotely generated tides to regional internal tidal field has been underscored through simulations (Mazloff et al., 2020; Ray & Zaron, 2016; Zhao et al., 2016).

Another factor that makes internal tides complicated off the U.S. west coast is their temporal variability. The impact of time-varying stratification and background currents on the generation and propagation of internal tides can occur over different time scales. It can happen over a short period of a few days or in longer time scales such as seasons and years. Interactions with mesoscale eddies and large-scale ocean circulations are suggested to be one of the main drivers of the temporal and spatial variation of internal tides (Kelly et al., 2016; Zaron & Egbert, 2014), leading to energy conversion, propagation speed and direction changes, and phase variations of internal tides (Huang et al., 2018; Rainville & Pinkel, 2006; Zilberman et al., 2011). Another influential factor is seasonal stratification, which affects internal tides in terms of incoherence, propagation direction, amplitude, and energy flux (Ansorg et al., 2017; Shriver et al., 2014; Zhao et al., 2012). However, seasonal variations of internal tides are not solely attributed to stratification, but also to the seasonality of other ocean processes (Buijsman et al., 2017; Qiu et al., 2014; Sasaki et al., 2014; Zhao, 2021). The CCS region exhibits seasonal variations in eddy kinetic energy and mean current patterns (Checkley & Barth, 2009; Haney et al., 2001; Rudnick et al., 2017). In addition, wave interference and the absence of comprehensive 4-dimensional observations hinder the way to dynamically link these main drivers to internal tide features (Buijsman et al., 2017), leading to incomplete understanding of temporal variations of internal tides. Here, using the three-step procedure (Zhao, 2022), we focus on investigating the seasonal variations of internal tides in the presence of mesoscale eddies off California, where a complex internal tidal field is seen from observations.

This study is also motivated by the availability of moored observation from the Surface Water and Ocean Topography (SWOT) mission pre-launch campaign in 2019 (Fu et al., 2024; Wang et al., 2022), and the latest advanced satellite altimetry model (Zhao, 2022) that is able to derive the seasonality of internal tides. The global climatological seasonality of internal tides was successfully extracted by subsetting altimetry sea surface height (SSH) data into four seasons, leveraging a mapping method that incorporates two key techniques: plane wave analysis and spatial band-pass filtering (Zhao, 2021; Zhao & Qiu, 2023). Characterized by its global coverage and minimal errors, the latest altimetry model enables a global assessment of seasonal variations of internal tides while offering a meaningful comparison with in situ observations and numerical simulations. Completing with short-term moored observations, satellite altimetry offers a unique perspective on internal tide in a complex ocean environment (Köhler et al., 2019; Löb et al., 2020). In our study region, where multisource internal tide interference patterns are present (Rainville et al., 2010), investigating internal tidal variations in different time scales necessitates the complementary use of moored and altimetry data.

This paper begins by investigating the temporal and spatial variations in modal composition and coherence of the semidiurnal internal tide observed by moorings. Our analysis focuses on the mode-1 and mode-2 M_2 internal tides, considering the influence of mesoscale eddies. We then proceed to examine the mean and seasonal variations of internal tides by analyzing waves from three directions using 27-year satellite altimetry observations. The preeminent seasonality of mode-1 tides is further explored quantitatively. Through this study, we aim to provide the characteristics of semidiurnal internal tides in different time scales in the CCS region.

This paper is organized as follows: Section 2 provides an overview of the data from the SWOT mission pre-launch campaign and processing methods. Section 3 introduces the satellite altimetry data and presents two key techniques utilized to extract the internal tidal signal. Section 4 presents the findings from the moored observations. Section 5 delves into the distinct generation and propagation characteristics of mode-1 and mode-2 M_2 tides from the satellite observations. The seasonality of mode-1 tides in the CCS region is further examined in Section 6. Finally, in Section 7, we summarize the results and draw our conclusions.

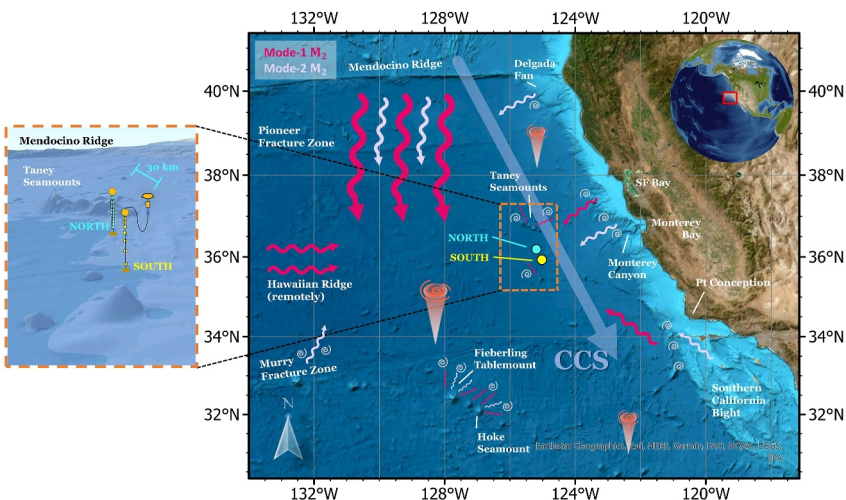


Figure 1. Study region in the California Current System (CCS). Bathymetry is mapped using data from GEBCO, with key topographic features labeled. Two moorings deployed during the Surface Water and Ocean Topography pre-launch campaign 2019 are labeled in cyan (the north mooring) and yellow (the south mooring). Major sources of mode-1 (red) and mode-2 (purple) M_2 internal tides in this region are marked as curved arrows, based on the 27-year-coherent satellite altimetry model. The figure in the left of an orange box is the zoom-in view of the two moorings 30 km apart.

2. SWOT Pre-Launch Field Campaign

2.1. Field Campaign

The SWOT Calibration/Validation (Cal/Val) pre-launch field campaign was carried out in a region located about 300 km west of Monterey, California, from September 2019 until January 2020 (Figure 1). Two moorings from the campaign are studied in this work; the PMEL/WHOI mooring was at 125.13°W , 36.12°N (hereinafter as “the north mooring” based on latitudinal position) and the Scripps Institution of Oceanography mooring was at 125.05°W , 35.85°N (hereinafter as “the south mooring”). Both moorings provide hydrographic temperature and salinity measurements, and bottom pressure from bottom pressure recorders. In addition, the surface buoy on the north mooring was equipped with a Global Positioning System sensor measuring the true SSH.

This study uses data from salinity, temperature, and pressure instruments on the north mooring and the south mooring. The north mooring has 18 fixed Conductivity, Temperature, and Depth (CTD) sensors located unevenly throughout the ocean column, measuring temperature, salinity, and conductivity with a sample interval of 1 min. The south mooring has a Wirewalker profiler equipped with Sea-Bird Electronics SBE37-IM and RBR Concerto, which crawls up and down along the mooring wire from the surface to about 500 m. They provide temperature and salinity measurements of the water column with a vertical resolution of about 29 m and deliver one up or down profile every 18.6 min on average. Below 500-m depth, eight fixed CTD are positioned unevenly toward the bottom with a sampling interval of 10 min. Figure 2a shows details of the instrument arrangements for both moorings. Further information on the data can be found in Wang et al. (2022).

2.2. Data Processing

The data obtained from 14 fixed CTDs at the north mooring are utilized after the quality control (see details in Supporting Information S1). A time period of 75 days, from yearday 251 (9 September 2019) to yearday 325 (22 November 2019), is chosen for both moorings. In this paper, yearday 251 is 00:00 UTC on 9 September 2019. To facilitate comparison, the data from the upper 500 m at the south mooring are gridded onto a uniform 1-hr temporal and 5-m vertical grid using linear interpolation. The vertical displacement is calculated by determining the potential density anomaly (σ) from temperature and salinity data using the Gibbs Sea Water Function and the Thermodynamic Equation of Seawater 2010 software (McDougall & Barker, 2011). Figure 3 illustrates the time series of potential density at the north mooring, while a similar figure for the south mooring can be found in the Supporting Information S1.

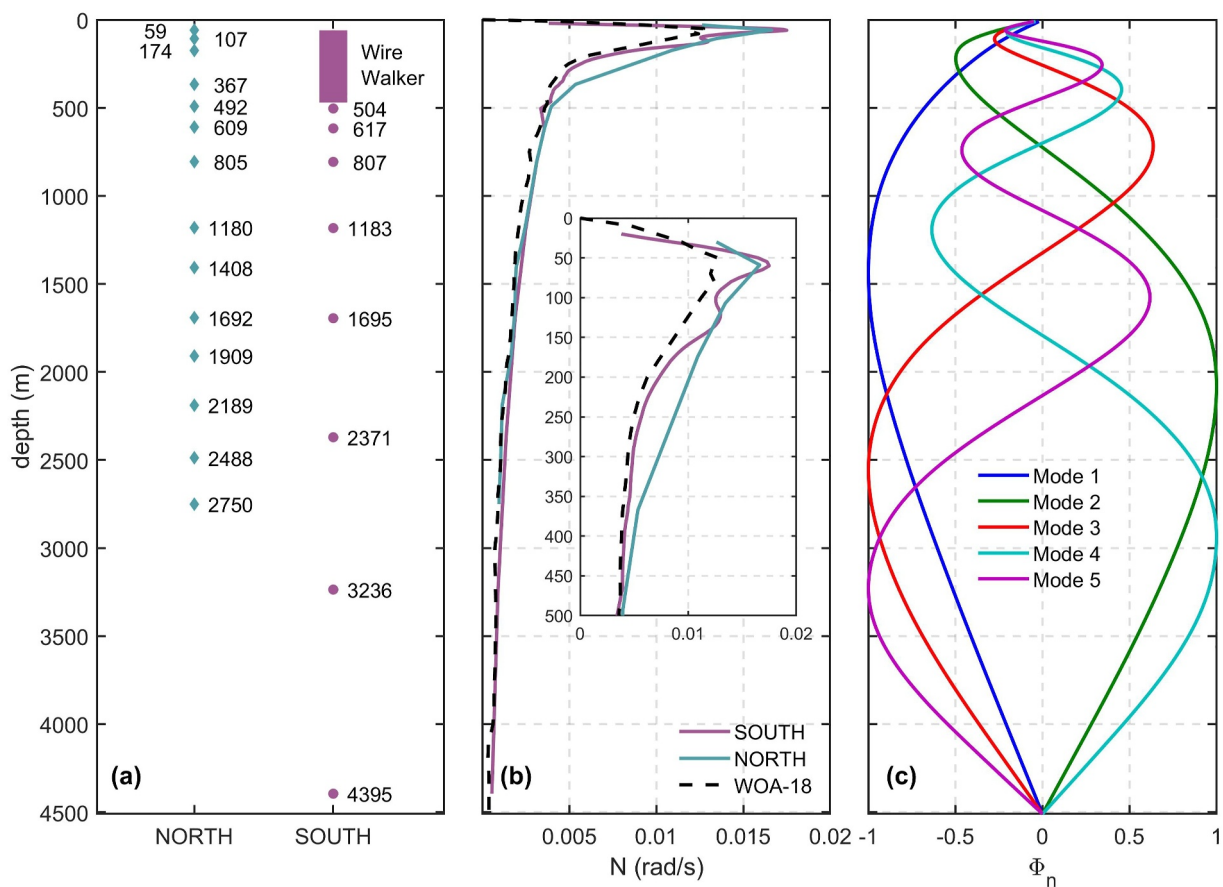


Figure 2. Mooring instrumentation and ocean stratification profiles. (a) The north mooring instruments (cyan diamonds as fixed Conductivity, Temperature, and Depth [CTDs]) and the south mooring instruments (magenta asterisks as fixed CTDs and the box as the Wirewalker Profiler). Depth (m) of each fixed CTD is provided. (b) Brunt–Väisälä frequency N profiles (in rad/s). The solid lines are mooring measurements (cyan for the north mooring and magenta for the south mooring). The black dashed line is the WOA18 annual mean hydrographic data. The close-up view is of the upper 500 m. (c) Normalized vertical structure of the first five baroclinic modes (in colors) of internal tides for vertical displacement.

The ocean conditions can be obtained by calculating the buoyancy frequency (N^2) using a CTD-profile created from the *World Ocean Atlas 2018* (WOA18) (Boyer et al., 2019). The dashed line in Figure 2b represents the stratification profile obtained from a climatological analysis. This profile aligns with the measurements from the two moorings (represented by solid lines), with the exception of the upper 500 m (as shown in the close-up view). In order to preserve the seasonal (fall) ocean condition in the CTD-profile, we use data acquired from the Wirewalker Profiler in the south mooring for the upper 500 m while data from WOA18 are employed for the remaining depth.

2.3. Vertical Displacement and Its Frequency Spectra

Displacement of isopycnal η_σ is computed by potential density profiles via the relation

$$\eta_\sigma(z, t) = \frac{\sigma'(z, t)}{\frac{d\sigma}{dz}} \quad (1)$$

The gradient of potential density $\frac{d\sigma}{dz}$ is from CTD-profile, which is built with data from WOA18 and Wirewalker Profiler. The perturbation is $\sigma'(z, t) = \sigma(z, t) - \bar{\sigma}(z)$, where $\sigma(z, t)$ is the instantaneous density anomaly and $\bar{\sigma}(z)$ is the time mean of the potential density anomaly profile over the entire 75 days. We adjust the displacement by removing the components of pressure variations arising from the mooring design (see details in Supporting Information S1).

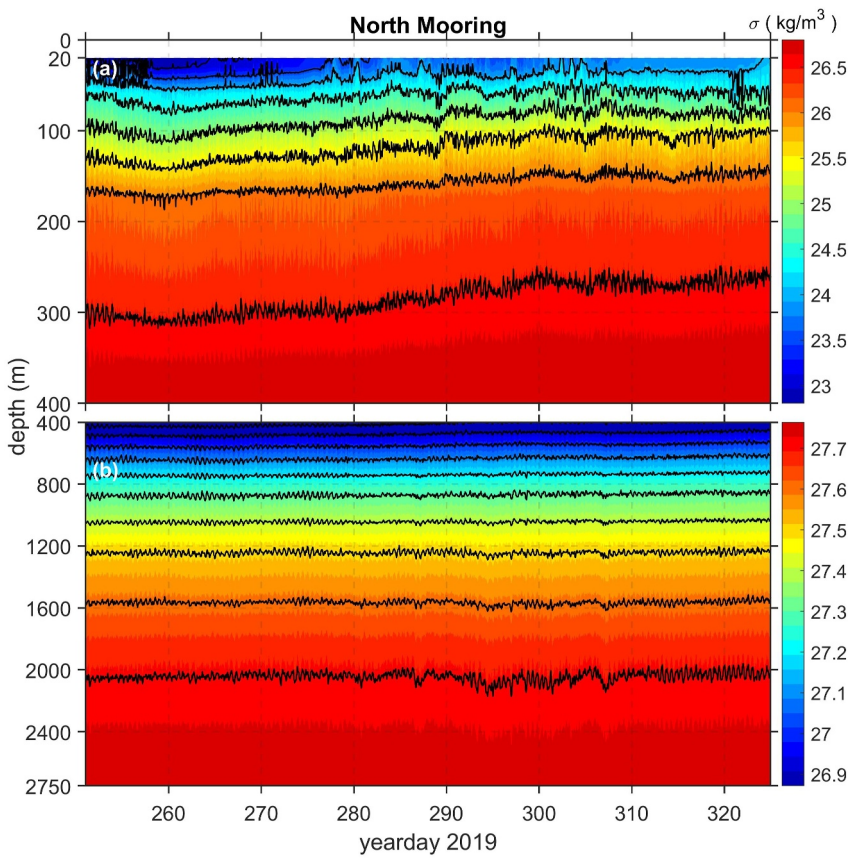


Figure 3. Hourly gridded potential density anomaly σ at the north mooring (a) at upper 400 m and (b) 400–2,750 m. Black contour lines are isopycnals with a constant density value. Note that there are different ranges of colormap for (a) and (b).

Figure 4 shows the spectrum of η_{tide} as a function of depth for the two moorings below the mixed layer in the upper ocean. The spectra are computed using a sine multitaper method (Thomson, 1982) with two sine tapers giving a degree of freedom of 4. A smoothing process is applied to geometrically smooth the spectrum over 1/250 of the total bandwidth. The resulting spectrum resolution is 0.0135 cycles per day. Strong semidiurnal tidal signals are apparent for both moorings. The nonlinearity of internal tides is indicated by the presence of overtones (i.e., M_4 in here) and some near-inertial motion (f) is also seen. It is worth noting that the potential-energy based analysis may underestimate the near-inertial component. The 95% and 50% confidence intervals of the spectrum can be referred in Supporting Information S1.

2.4. Band-Pass Filtering and Harmonic Analysis

The temporal variability of each tidal component is examined by band-pass filtering via fourth-order Butterworth and harmonic analysis. This passing band includes M_2 and S_2 tidal constituents and is referred to Zhao et al. (2010)'s set up, which is centered at the M_2 tidal frequency ($2.23 \times 10^{-5} \text{ s}^{-1}$) with zero-phase response and quarter-power points at $2.01 \times 10^{-5} \text{ s}^{-1}$ and $2.47 \times 10^{-5} \text{ s}^{-1}$, that is, 1.73–2.13 cpd. These frequency limits are wide enough to capture the majority of semidiurnal signals but narrow enough to separate them from other nontidal motions. The available data record is long enough to perform this filtering without being concerned with leakage or ringing, which are artifacts that can occur in the filtered signal due to the finite length of the data record and the characteristics of the filter.

The band passed semidiurnal signals are a combination of M_2 , S_2 , N_2 and incoherent constituents. The 75-day data record is long enough to separate M_2 , S_2 , and N_2 so that they can be extracted by harmonic analysis (Pawlowicz et al., 2002). As coherent M_2 , S_2 , and N_2 signals dominate, K_2 constituent is neglected. The baroclinic vertical displacement is expressed as

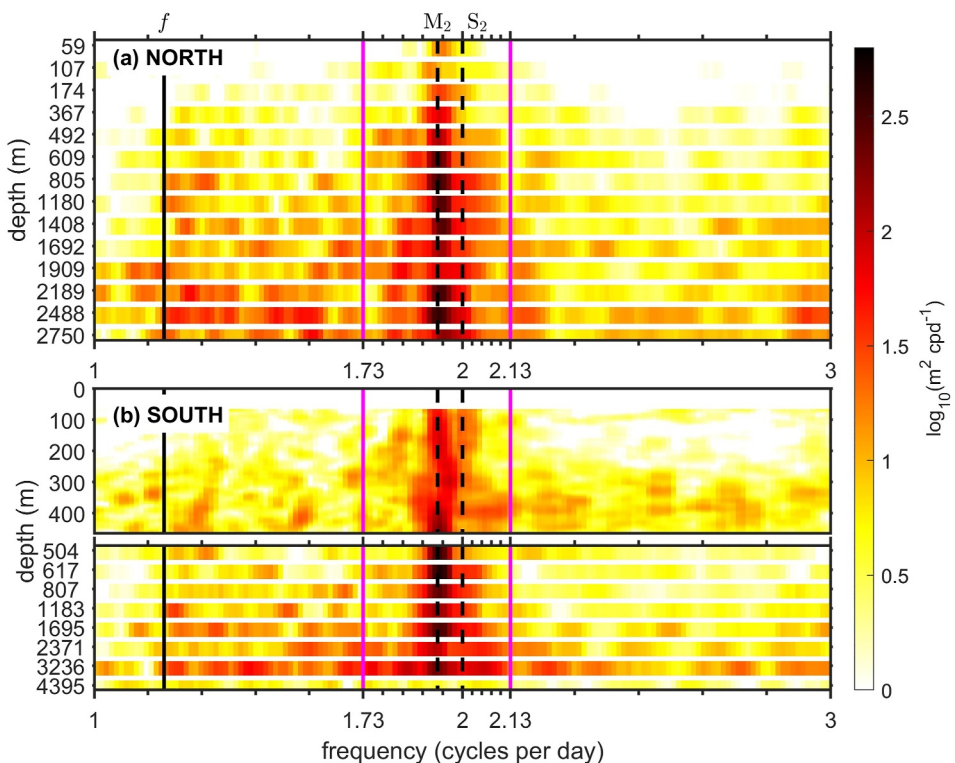


Figure 4. Spectrum of tidal displacement of (a) the north mooring and (b) the south mooring at depth of every Conductivity, Temperature, and Depth sensor. The spectra are calculated using a sine multitaper method giving a degree of freedom (DOF) of 4. A smoothing process is applied to geometrically smooth a spectrum, covering over 1/250 of the total bandwidth. Major frequency are labeled: M₂ and S₂ are as dashed black lines, inertial frequency is as a solid black line, and band-pass limits are as solid magenta lines.

$$\eta'_{semi} = \eta'_{M_2} + \eta'_{S_2} + \eta'_{N_2} + \eta'_{in} \quad (2)$$

where η'_{in} indicates the incoherent portion, unresolved coherent tides, and noise.

2.5. Modal Decomposition

Internal tides can be described by a superposition of discrete baroclinic modes that, for horizontally uniform $N(z)$ and no background shear, propagate as linear waves. Therefore, to analyze the semidiurnal vertical displacement within the chosen frequency band, displacement is projected onto these baroclinic modes. As described by Zhao et al. (2016), the baroclinic modes for vertical displacement, $\Phi(z)$, are calculated by the eigenvalue equation (Munk, 1981; Wunsch, 1975),

$$\frac{d^2\Phi(z)}{dz^2} + \frac{N^2(z)}{c_n^2}\Phi(z) = 0 \quad (3)$$

We use free-surface boundary conditions with a flat bottom. Subscript n is the vertical normal mode number and c_n is the eigenvalue velocity (Gill, 1982). $N(z)$ is taken from the CTD-profile, which is built with data from WOA18 and Wirewalker Profiler. The energy estimates can be severely limited by vertical gaps in the measurements, but it is possible to represent internal tides by combining several distinct baroclinic modes (Nash et al., 2005; Zhao et al., 2012). The water column coverage is sufficient to compute the lowest five vertical modes, as shown in Supporting Information S1.

The modal structure of horizontal velocity and pressure $\Pi(z)$ can be described as (Gill, 1982)

$$\Pi(z) = \rho_0 c_n^2 \frac{d\Phi(z)}{dz} \quad (4)$$

ρ_0 is the vertically averaged water potential density.

After computing five-mode solutions for both moorings, the baroclinic displacement is expressed as

$$\eta'(z, t) = \sum_{n=1}^5 \eta'_n(t) \Phi_n(z) \quad (5)$$

where $\Phi_n(z)$ represents the vertical structure of the n th baroclinic mode and $\eta'_n(t)$ is the time-varying displacement of the n th baroclinic mode. At each time, $\eta'_n(t)$ is determined by least squares modal fitting.

Depth-integrated available potential energy (APE) is determined by the baroclinic displacement $\eta'(z, t)$

$$APE = \frac{1}{2} \rho_0 \int_{-H}^0 \langle N^2(z) \eta'^2(z, t) \rangle dz \quad (6)$$

with the unit of J/m^2 , where the angle brackets are the average over one tidal cycle, ρ_0 is the vertically averaged water potential density, and $N(z)$ is the buoyancy frequency from the CTD-profile. Horizontal kinetic energies and flux (F) are unavailable due to a lack of moored measurement of baroclinic current velocity $\mathbf{u}(z)$.

In order to compare with satellite altimetry, the sea surface height anomalies (SSHAs) are calculated with interior isopycnal displacement for each mode η'_n derived from above, which can be expressed as

$$SSHA_n = \kappa \eta'_n(t) \quad (7)$$

which κ is the conversion ratio depending on latitude, mode number, and frequency.

$$\kappa = \frac{1}{g} \int_{-H}^0 N^2(z) \Phi(z) dz \quad (8)$$

For details, please refer to Appendix A in Zhao et al. (2016). $\kappa = 1.1 \times 10^{-3}$ for M_2 mode-1 tide and $\kappa = 0.7 \times 10^{-3}$ for M_2 mode-2 tide in this site. For convenience, SSHAs are then converted from meters to millimeters.

3. Satellite Altimetry Model

Two kinds of satellite altimetry models are used in this study: the 27-year-coherent model and the climatological seasonal model.

3.1. Satellite Altimetry Data

Following the new mapping technique described in Zhao and Qiu (2023), the regional M_2 internal tidal field is mapped using 27 years (1993–2019) of satellite data from multiple altimetry missions. The SSH data from seven exact-repeat satellite missions are combined into four data sets based on their orbital configurations, including 254 tracks from TOPEX/Poseidon-Jason, 254 tracks from TOPEX/Poseidon-Jason tandem, 1002 tracks from European Remote Sensing Satellite-2, and 488 tracks from Geosat Follow-On. The merged data sets have denser ground tracks and higher spatial resolution compared to each individual mission with sparse tracks, enabling the development of an accurate internal tide model. Previous studies (Zhao, 2021; Zhao & Qiu, 2023) used the same data, except with a 25-year (1993–2017) altimetry record. Standard corrections are applied to all SSH measurements to address atmospheric effects, surface wave bias, and geophysical effects. The corrections for the ocean barotropic tide, polar tide, solid Earth tide, and loading tide are conducted using theoretical or empirical models.

3.2. Mapping Procedure and Techniques

Two key techniques, plane wave analysis and 2D spatial filtering, are applied to the mode-1 and mode-2 M_2 mapping procedures. Instead of point-wise harmonic analysis, plane wave analysis (Zhao, 2016; Zhao et al., 2016) extracts internal tides by fitting plane waves using all altimetry measurements in one given fitting window that is 160 km in width. In overlapping fitting windows, least squares fitting is used to calculate the amplitudes a , phases ϕ , and propagation directions θ of the target internal tidal waves, following

$$\eta(x, y, z) = \sum_{m=1}^M a_m \cos(kx \cos(\theta_m) + ky \sin(\theta_m) - \omega t - \phi_m) \quad (9)$$

where ω and k are the frequency and wavenumber of M_2 , x and y are the local Cartesian coordinates, and t is the time. M is the number of internal waves extracted in each window via an iterative algorithm. Five waves are fitted for both mode-1 mode-2. Then M_2 internal tides are mapped at regular spatial grids.

2D spatial filtering aims to remove higher baroclinic modes and nontidal noise by employing a horizontal band-pass filter. The filter has a bandwidth of [0.8 1.25] times the regional mean wavelength, which is tested empirically with several values. For this method to work effectively, it is crucial that the variance of internal tides is mostly around the theoretical wavenumber (Zhao et al., 2019). The wavelength (wavenumber) of M_2 internal tides depends on factors such as ocean depth, latitude, mode number, and ocean stratification. In Section 3.3, we will address the determination of this prerequisite parameter, with particular emphasis on accounting for seasonal variation.

The 27-year-coherent internal tide model is constructed following the mapping procedure described in Zhao and Qiu (2023), which involves three steps: (a) plane wave analysis to map internal tides at a 160×160 km window with five waves, (b) 2D spatial filtering to clean internal tides based on wavenumber, (c) multidirectional decomposition using plane wave analysis within the same window as step (a) to separate tidal waves by propagation directions. In the end, the internal tidal field is mapped on the grid of $0.1^\circ \times 0.1^\circ$ for mode-1 and $0.05^\circ \times 0.05^\circ$ for mode-2. The resultant tidal models exhibit minimal error, making it possible to resolve weak seasonal signals of internal tides from different propagating directions.

3.3. Seasonal Data Subsetting

The climatological seasonal internal tide models are built with four seasonal subsets of altimetry data and WOA18 climatologies, following the method from Zhao (2021). The four seasonal subsets consist of January, February, and March for the winter model, April, May, and June for the spring model, July, August, and September for the summer model, and October, November, and December for the fall model. The seasonal models are developed following the same mapping procedure as the 27-year-coherent one, but with the respective data subset. Zhao (2021) employed this approach to study the seasonality of M_2 mode-1 internal tides.

To consider the seasonal variations from the altimetry models, the M_2 wavelength (wavenumber), one of the prerequisite parameters, is calculated for the four seasons using the ocean stratification profiles from the WOA18 climatological seasonal hydrography. At each $0.25^\circ \times 0.25^\circ$ grid point of the WOA18 data set, the vertical structure and wavelengths are determined by solving the Sturm-Liouville orthogonal Equation 3 and $\lambda = \frac{c_n^2}{\omega}$. The largest mode-1 M_2 internal tides are our focus for seasonality analysis.

3.4. Energetics

The depth-integrated energy flux can be calculated from the satellite-derived SSHAs following

$$Flux = \frac{1}{2} a^2 F_n(\omega, H, f, N) \quad (10)$$

where a is the SSH amplitude. This equation (Zhao, 2018; Zhao et al., 2016) involves the transfer function F_n , which is the other prerequisite parameter dependent on the frequency ω , water depth H , local inertial frequency f , and stratification N . The transfer function is derived using the hydrographic profiles from the WOA18 data set and can be calculated by

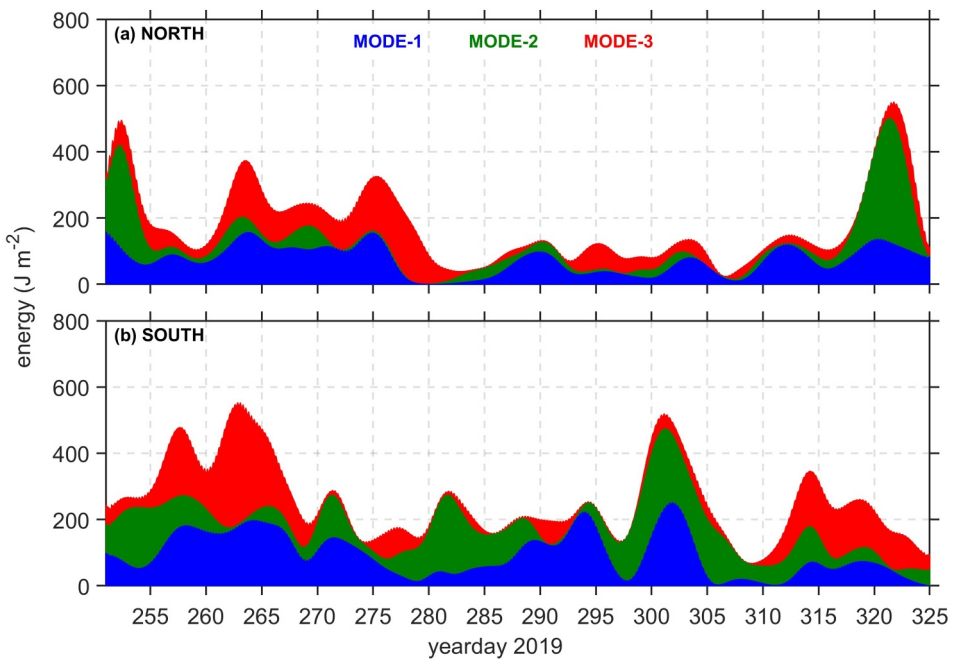


Figure 5. Time series of semidiurnal internal tide vertically integrated available potential energy (APE, J m^{-2}) in modes 1–3 (stacked colors) at (a) the north mooring and (b) the south mooring. Temporal variations of semidiurnal internal tides are seen from both moorings.

$$F_n = \frac{\rho_0 g^2 \omega k_n}{\omega^2 - f^2} \int_{-H}^0 \Pi_n^2(z) dz \quad (11)$$

The wavenumber $k_n = \frac{(\omega^2 - f^2)^{1/2}}{c_n}$ is derived following the dispersion relation. For details, please refer to Appendix A in Zhao et al. (2016). Since there are five waves at each grid point, the total values we discuss later are the scalar (energy) and vector (flux) sums of these waves.

4. Mooring Observations

In this section, we will present the observed time-varying internal tide energy of different modes and constituents at the two moorings. Our results indicate that (a) there are significant temporal and spatial variations of internal tides in the region. (b) The south mooring has a greater semidiurnal tidal energy, while the north mooring has a higher amplitude of M_2 mode-1 internal tide. (c) Mesoscale eddies likely contribute to the temporal variations.

4.1. Time Series

To evaluate the temporal variations of internal tides at each mooring and their spatial disparities, we compute the vertical-integrated APE from baroclinic displacement η in mode 1–3 using Equation 6. The time-averaged energy in each mode at the south mooring is higher than at the north mooring. At the north mooring (Figure 5a), the energy in the lowest-three modes is 178 J/m^2 . Contrary to the expected case described by de Lavergne et al. (2019), which suggests a strong decay of both energy and conversion rate with increasing mode number, we find that mode-3 tide (56 J/m^2) and mode-2 tide (49 J/m^2) are of similar magnitude. We acknowledge that there are uncertainties in estimating the modal contribution due to observations characterized by incomplete vertical spatial coverage. Therefore, we focus only on mode-1 and mode-2 internal tides here (represented by blue and green colors in Figure 5). In addition, we conduct a sensitivity test about the modal fitting (see Supporting Information S1) to reduce the impact from defects in the measurement. Overall, it is clear that the majority of the measured energy is contained in low-mode tides (i.e., mode 1–3 with 81%). At the south mooring (Figure 5b), the energy of the total lowest-three modes is 225 J/m^2 and the energy decreases inversely to mode number. These

variations of energy for dynamics over a separation scale of $\mathcal{O}(30)$ km between the two moorings indicate a spatially complex internal tidal field in this region.

At both moorings, the internal tides have significant temporal variations. At the north mooring, there are specific periods, such as those spanning yeardays 257–265 and yeardays 315–325, exhibit synchronized changes among different tidal modes. Conversely, during other periods like yeardays 266–272 and yeardays 277–285, tides in different modes manifest incoherent behavior, signifying a lack of consistent temporal alignment. Even when the changes in different tidal modes align, these temporal changes are not necessarily in proportion. For instance, despite mode-1 predominating over the whole period, mode-2 (green in Figure 5a) gets excited during yeardays 315–325, which could be attributed to fluctuations in the background currents and eddies. Substantial variations in the energy time series are also evident at the south mooring. During certain periods, such as yeardays 268–272 and yeardays 295–305, there is consistency in how energy changes in different modes. However, overall, energy variations in different modes often do not follow a coherent or synchronized pattern, indicating temporal incoherence. We did not see an obvious spring-neap cycle of semidiurnal tides from the time series of both moorings, which is likely due to the extremely weak S_2 tide. According to satellite observations (see Section 5), S_2 is associated with an SSH signal of ~ 2 mm, while M_2 signal is ~ 10 mm in this region.

The temporal variations of mode-1 from two moorings are more visually similarly to those of mode-2. Mode-1 tides, for example, weaken around yearday 280 and get stronger afterward for both moorings. In contrast, the peak of mode-2 tides from the north mooring at around yearday 322 is not seen from the south mooring. Though neither of the correlations of temporal variability between the two sites are statistic significant, internal tides vary spatially in 30 km. If the observed tides from these two moorings were only from the Mendocino Ridge in the north, we would not expect to see such significant spatial differences, especially for mode-2 tides. Therefore, we argue that these spatial variations are contributed by multiwave interference and different generation sites for mode-1 and mode-2 tides. This argument will be investigated with satellite observations in the next section.

4.2. Tidal Constituents

We employ harmonic analysis to assess the energy of different semidiurnal tidal constituents, including M_2 , S_2 , and N_2 . The coherent and incoherent portions are defined in Section 2.4. The coherence of internal tides varies with different modes due to their unique vertical structure and propagation velocity (Ponte & Klein, 2015; Rainville & Pinkel, 2006). Therefore, investigating the coherence of internal tides mode-by-mode is necessary. To achieve this, we utilize modal decomposition techniques.

M_2 tides are dominant for mode-1 and mode-2 tides at both moorings. At the north mooring (Figures 6a and 6b), M_2 is dominant with 84 J/m^2 (38% of total semidiurnal energy), while S_2 and N_2 are only 6 J/m^2 (3%) each. M_2 also has the highest partition of energy among all semidiurnal constituents for each mode. Similarly, at the south mooring (Figures 6c and 6d), M_2 has the greatest partition with 113 J/m^2 (33%), compared to 30 J/m^2 (9%) for S_2 and 12 J/m^2 (3%) for N_2 . Considering constituent partitions in each mode, M_2 is dominant in both mode-1 (48%) and mode-2 (49%). Although the total semidiurnal tide energy is higher at the south mooring, M_2 mode-1 energy is higher at the north mooring.

Both moorings exhibit a large incoherent portion (yellow columns in Figure 6). The incoherent portion (129 J/m^2 , 57% at the north mooring, 187 J/m^2 , 55% at the south mooring) is higher than any single constituent and exceeds the total amount of all coherent components. This large incoherent portion is probably caused by the influence of California currents and eddies, which decrease the coherent fraction of tidal energy by wave refraction (Rainville & Pinkel, 2006). Nontidal noise, such as that arising from the “swing” mooring configuration and the relatively short observation period (~ 3 months), could also contribute to the large incoherent portion. In particular, the incoherent part of mode-3 at the south mooring, which accounts for over 87% of the total energy in that mode, is likely unrealistic and could be the result of nontidal noise. The “real” incoherent portion of the internal tide is unreliable when the signal-to-noise ratio is low. Besides, fast-sampling instruments would reduce the errors from unresolved tidal signal. Overall, the observed incoherent tides from both moorings are close to the globally-averaged 45% (Zaron & Ray, 2017) or 49% (Nelson et al., 2019) semidiurnal nonstationary variance fraction.

In terms of M_2 tides, mode-1 (69%) dominates mode-2 (10%) tides at the north mooring while mode-1 (48%) and mode-2 (49%) tides are comparable at the south mooring. In addition, mode-1 tides have similar energy levels

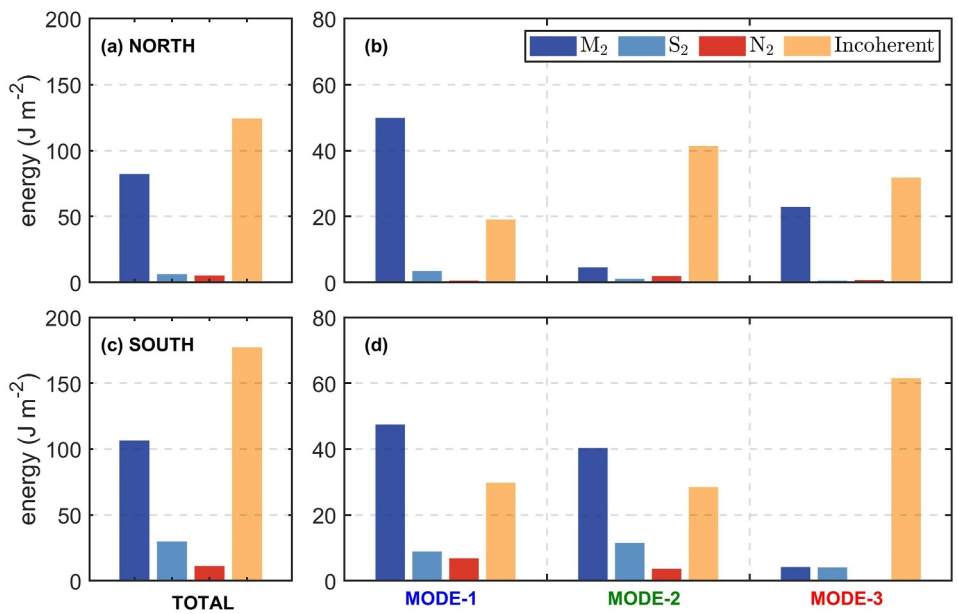


Figure 6. (a) Partition of energy by tidal constituents at the north mooring. Modal decomposition is applied to each tidal constituent and (b) shows the partition on the lowest-three modes (in the x axis). The same analysis for the south mooring is presented in (c) and (d).

between the north mooring (50 J/m^2) and the south mooring (46 J/m^2). However, relatively strong mode-2 M_2 tides with 44 J/m^2 are observed at the south mooring, compared to 5 J/m^2 at the north mooring. Thus mode-2 changes more than mode-1 between the two moorings. We speculate that mode-1 is similar due to the dominance of the source at the Mendocino Ridge. In contrast, mode-2 has multiple, interfering sources, leading to rapid spatial changes on scales less than the wavelength, as suggested by Wang et al. (2022).

4.3. The Impact of Mesoscale Eddies

In our previous discussion, we suggested the contribution of mesoscale currents and eddies to the incoherent component of internal tides. Here, we will explore this statement in more detail. Wang et al. (2022) detected the development of a warm-core anticyclonic mesoscale eddy from the mooring array during the pre-launch campaign. The two moorings were within the meander on 8 September and on the edge of the formed eddy by the end of the deployment on 24 November (Figure 7). The formation of this eddy coincides with the different temporal variations of energy in different semidiurnal modes (Figure 5). The phase velocity of internal waves is dependent on the ocean stratification. Therefore, we derive the phase velocity of mode-1 tides using the moored observation (see the method in Supporting Information S1) showing a strong correlation between the phase speed and the SSH. Assuming a generation site at the Mendocino Ridge and using the AVISO absolute dynamic topography (ADT), we find a change in mode-1 phase speed of 3.12 m/s and a standard deviation of 0.03 m/s during the mooring deployment.

This analysis shows that mesoscale eddies are likely responsible for an increased travel time ($\sim 1 \text{ hr}$) of mode-1 tides from the Mendocino ridge to the mooring locations. This is equivalent to about 30° of phase change. However, this does not completely explain the observed variations in tidal energy; a variation of about 90° is probably necessary as well as much more rapid changes in phase. Furthermore, the lack of comprehensive in-situ data and the effect of multiple sources of internal tides with equal contributions, make it challenging to provide a more quantitative picture here. We expect response of mode-2 or higher mode tides to eddies to be stronger (Dunphy et al., 2017; Löb et al., 2020). Additional research to detail the mechanism of wave-mesoscale interaction is needed. Ongoing researches involve both numerical simulations and theoretical analyses, focusing on topics such as internal tide advection and refraction, enhanced dissipation of low-mode tides, and upscale energy transfer (Rainville & Pinkel, 2006; Savage et al., 2020; Shakespeare, 2023). These studies inspire the design of

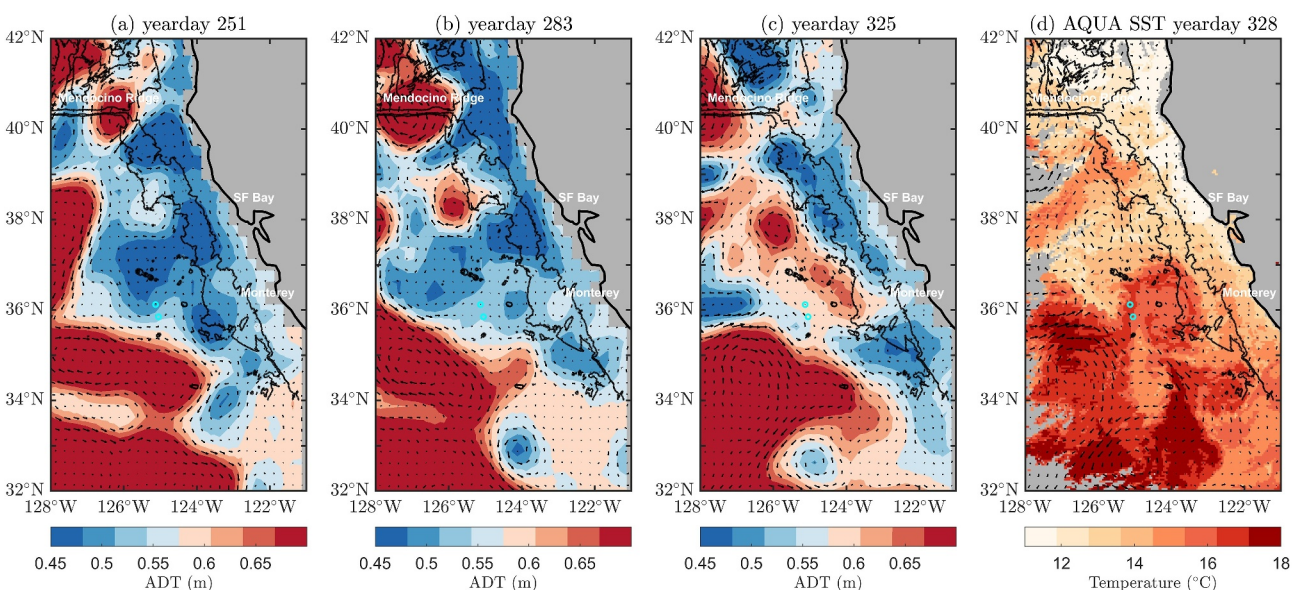


Figure 7. The absolute dynamic topography (ADT, color) and the surface geostrophic velocity anomaly (arrows) on (a) 8 September (yearday 251), (b) 10 October (yearday 283), and (c) 21 November (yearday 325), corresponding to the start, middle, and end of the pre-launch campaign in 2019. The ADT and surface geostrophic velocity field are from the Copernicus Marine Service (European Union-Copernicus Marine Service, 2021). The cyan-colored dots mark the locations of the two moorings. A warm-core anticyclonic mesoscale eddy was formed close to the moorings. (d) The sea surface temperature (SST) after the formation of an eddy around November 24 (yearday 328), supporting the existence of an anticyclonic eddy. The SST data are MODIS Aqua Level 3 SST MID-IR Daily 4 km product, from the Physical Oceanography Distributed Active Archive Center (PO.DAAC) (NASA/JPL, 2020). Surface geostrophic velocity fields are provided for reference. Contours for the 3,000 and 3,800-m isobath are shown.

future field programs that seek evidence for validation and potential adjustments for the parameterization and approximation in these theoretical and numerical models.

5. Comparisons With Satellite Observations

To better comprehend the internal tide in different temporal scale in this region, we compare moored observations with internal tide models that are based on 27 years of satellite altimetry data. Our findings are as follows: (a) the amplitude and phase of both mode-1 and mode-2 M_2 internal tides extracted from the moorings are in good agreement with those obtained by satellite observations. (b) Despite the two moorings being only 30 km apart, there are spatial variations of M_2 internal tides due to interference from waves arriving from all directions. (c) We observe different features of mode-1 and mode-2 M_2 internal tides, resulting from distinct generation sites. Specifically, mode-1 tides mainly originate from the Mendocino Ridge and 36.5–37.5°N California continental slope, while mode-2 tides primarily come from local seamounts and Monterey Bay.

5.1. Altimetry Result

The SSHAs of mode-1 and mode-2 tides, derived from the 27-year-coherent M_2 altimetry model described in Section 3, reveal a complex internal tidal field in the studied region (Figure 8). This complexity is attributed to the presence of multiple sources for internal tides in the region, including the Hawaiian Ridge, the California continental slope, the Mendocino Ridge, and local generation over nearby seamounts. The superposition of multi-directional waves leads to the formation of standing-wave patterns. For mode-1 (Figure 8a), the predominant tidal waves propagate in north-south direction, originating from the Mendocino Ridge. Though the Mendocino Ridge is also a significant source for mode-2 tide (Figure 8b), the southward waves have a shorter excursion and do not reach the moorings location (cyan circles). Instead, the main sources of mode-2 at the two moorings are tidal beams originating from Monterey Bay and the Southern California Bight (SCB). However, the interference of multiple waves limits us to accurately determine the propagation direction of individual tidal beam and quantify its energy. Employing the multiwave decomposition approach is the key to overcoming the challenge and its effectiveness has been demonstrated in prior research (Zhao & Qiu, 2023).

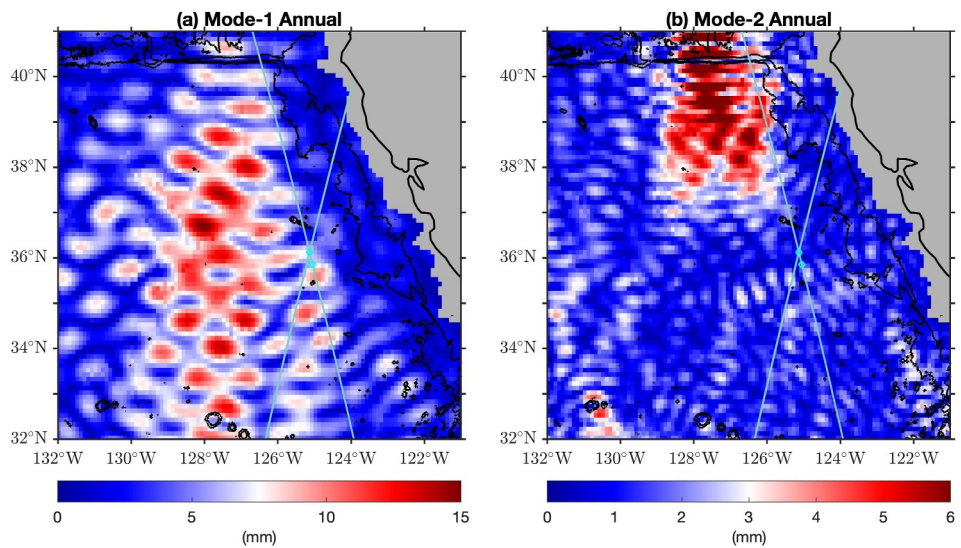


Figure 8. The sea surface height anomalies of M_2 (a) mode-1 and (b) mode-2 internal tides from the 27-year-coherent altimetry model. Note that different colorbar ranges are used for mode-1 and mode-2. Two cyan circles show the location of the two moorings from the Surface Water and Ocean Topography pre-launch campaign. Two cyan lines crossing the north mooring are Sentinel-3A satellite tracks (S3A-140 and S3A-318). Contours for the 3,000 and 3,800-m isobath are shown.

The altimetry model offers a two-dimensional perspective on the generation and propagation of internal tides, which provides valuable context for interpreting the pointwise information obtained from mooring measurements. As such, the combination of these two data sets allows for a more comprehensive and nuanced analysis of the internal tidal field. For instance, the altimetry model can provide valuable insights into the spatial distribution of the mode-1 tidal beam and its relation to the mooring locations. This information can support the interpretation of the relatively small tidal amplitudes observed at the moorings, considering their proximity to the edge of the mode-1 tidal beam (Figure 8a). However, before delving into the detailed analysis, it is essential to establish the coherence and reliability of the two data sets to confidently utilize the altimetry model to shed light on the mooring observations.

5.2. Comparison With Moored Data

We compare the amplitude and phase of M_2 tides at the two mooring locations from moored and satellite altimetry observations. Given the very different time scales of the satellite and moored data, agreement is surprisingly good from Figure 9. Our analysis focuses on mode-1 and mode-2 M_2 signals due to their substantial energy content and their strong detectability through satellite observations.

The moored mode-1 M_2 tides (Figures 9a and 9b) exhibit an amplitude of 4.8 mm and a phase of 208° at the south mooring. At the north mooring, the corresponding values are 5.1 mm and 121° , both with a 95% confidence interval. The extraction of mode-2 M_2 tides poses greater challenges compared to mode-1 tides due to their relatively small amplitude and stronger seasonal variability. The moored mode-2 M_2 tides (Figures 9c and 9d) display an amplitude of 3.4 mm and a phase of 236° at the south mooring. At the north mooring, the corresponding values are 1.1 mm and 146° , both with a 95% confidence interval.

Comparatively, the satellite altimetry models, depicted as black triangles for the 27-year-coherent model and cyan bars for the seasonal models (only mode-1 tides), demonstrate a good agreement with the moored data. The amplitude and phase of seasonal models cover a reasonably wide range. However, it is challenge to drawing definitive conclusions from this comparison, no matter the altimetry models match well with the moored results or not. The two data sets differ in record length and provide information of internal tides in different time scales. The record length influences the partitioning between incoherent and coherent signals. The altimetry observations used in the model span a much longer period (27 years) compared to the limited 3-month duration of the moored data. Extended observations (altimetry results here) enable the analysis to filter out the temporally variable component, resulting from interaction with other ocean dynamics and changing stratification, thus leading to bias-

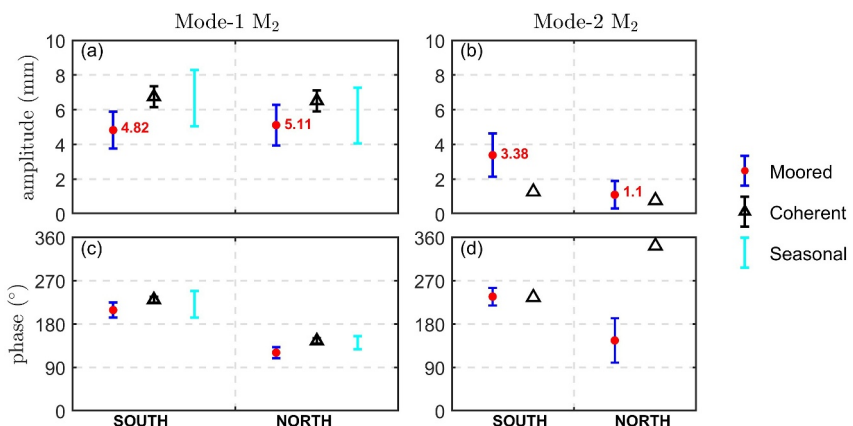


Figure 9. Comparison of moored and altimetry baroclinic sea surface height anomalies (SSHAs). (a) The amplitude (mm) and (c) phase (°) of mode-1 M_2 SSHAs. The moored data, shown as the band-pass filtered signal in Figures 6b and 6d, are represented by red dots with a 95% confidence interval as blue bars here. The amplitude is labeled explicitly. The black triangles depict results from the 27-year-coherent internal tide model. The black error bars for the 27-year-coherent model are ± 0.6 mm for amplitude and $\pm 6^\circ$ for phase. Four climatological seasonal internal tide models span a range in cyan. The tidal features at the south mooring are plotted in the left column and those at the north mooring are in the right column. (b) The amplitude (mm) and (d) phase (°) of mode-2 M_2 SSHAs.

low result. Furthermore, the altimetry measurements rarely capture the tidal variability associated with the advection and refraction caused by mesoscale eddies and currents. In addition, the modest amplitude of mode-2 tides renders them more susceptible to noise. Nevertheless, this comparison aims to furnish quantitative insights into internal tides across different time scales.

5.3. Generation and Propagation of Mode-1 and Mode-2 Tides

Consistent findings from both moorings and altimetry models reveal significant spatial variations of M_2 tides between the two moorings. In order to further investigate the altimetry results, we employ the 2D spatial filtering and plane wave analysis methods (Section 3). This method enables us to decompose the internal tidal field into different distinct propagation directions, providing a more detailed perspective on individual waves. Here, we decompose the 27-year-coherent altimetry results into three directions based on the dominant generation sites. Mode-1 tides are decomposed into southward waves (235° – 325°) from the Mendocino Ridge, eastward waves (-35° – 45°) from the Hawaiian Ridge, and northwestward waves (45° – 235°) from the local seamounts and continental slope. Mode-2 tides are decomposed into southward waves (245° – 325°) from the Mendocino Ridge, westward waves (125° – 245°) mostly from the continental slope, and northeastward waves (-35° – 125°) from the local seamounts. Through this decomposition, we are able to isolate and examine each wave, eliminating the interference caused by multiple waves (Zhao et al., 2019).

The mode-1 and mode-2 M_2 internal tides originate from different generation sites, based on the 27-year-coherent internal tide model. Mode-1 tides predominantly come from the Mendocino Ridge at 40.4°N , exhibiting a clear southward wave signal as depicted in Figure 10a. These waves propagate through both moorings, thereby explaining the relatively strong covariance observed in the moored data (Figure 5). These southward mode-1 waves are consistent with the previous in situ observation in this region (Alford, 2010; Musgrave et al., 2017). Interestingly, our analysis also indicates that local seamounts do not significantly contribute to the southward propagation of mode-1 tides, suggesting that these dominant and relatively larger mode-1 are not sensitive to minor topographic features. Internal tides from the California continental slope propagate northwestward (Figure 10b). Specifically, waves come from the SCB and the 36.5 – 37.5°N continental slope. In addition, two moorings are affected by the eastward tidal waves from Hawaiian Ridge (Figure 10c).

However, the behavior of mode-2 tides presents a different story. As illustrated in Figure 10d, the southward flux of mode-2 tides originating from the Mendocino Ridge (40.4°N) diminishes around 36.5°N . This finding is consistent with the simulation obtained from MITgcm in Zhao et al. (2019), indicating that the southward mode-2 tide propagates only a quarter of the distance covered by the mode-1 tide. Consequently, unlike mode-1 tides,

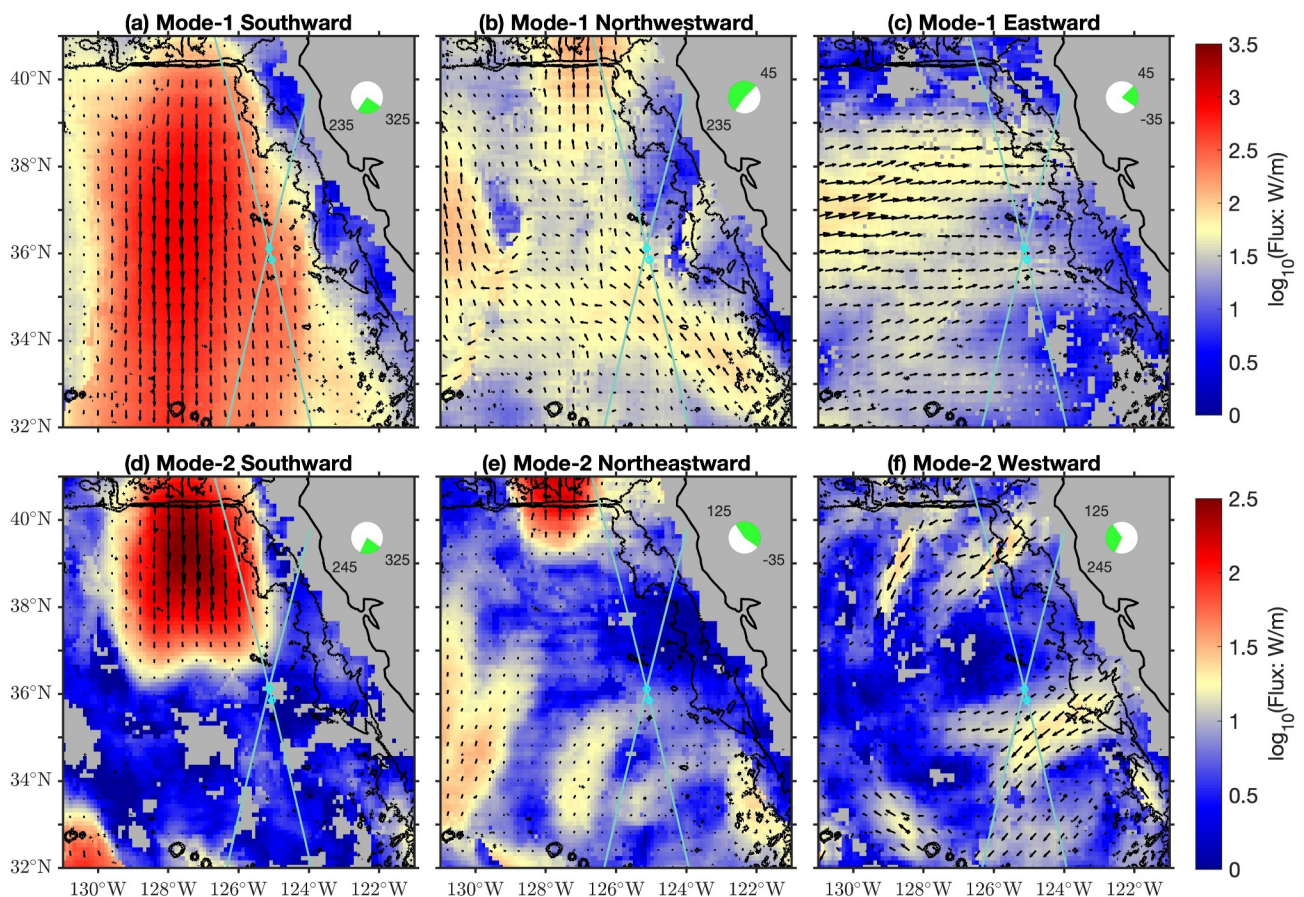


Figure 10. Fluxes of regional (a–c) mode-1 and (d–f) mode-2 M_2 internal tides from the 27-year-coherent model are shown in logarithmic scale. The internal tidal field has been decomposed into three components by propagation direction (directional range is shown as a green pie chart in the right upper corner). Colors and arrows indicate the magnitude and direction of internal tides, respectively. Note that different color bar ranges are used for different modes. Two cyan circles show the location of the two moorings from the Surface Water and Ocean Topography pre-launch campaign. Two cyan lines crossing the north mooring are Sentinel-3A satellite tracks (S3A-140 and S3A-318). Contours for the 3,000 and 3,800-m isobath are shown.

southward mode-2 tides have minimal impact on the mooring locations, likely due to dissipation or scattering processes. The role of bottom topography in far-field internal tide energy dissipation is prominent (de Lavergne et al., 2019; Kelly et al., 2013). The tidal dissipation are also shaped by the mode number, which governs the vertical structure, group velocity, and wave-wave interaction (Olbers, 1983; Onuki & Hibiya, 2018). Therefore, mode-2 exhibits heightened shear within its vertical scale compared to mode-1. Moreover, the propagation and decomposition of internal tides can be modified by the shear, strain, and varying stratification of background currents (Buijsman et al., 2017; Dunphy et al., 2017; Kelly et al., 2016; Polzin, 2008). Considering the relative energy levels, with mode-2 being weaker than mode-1, the southward mode-2 tides from the Mendocino Ridge tend to convert energy to higher modes more readily, leading to intensified dissipation via shear/advection instabilities (Kunze & Toole, 1997). Alternatively, energy transfer with background currents can also occur through interactions.

Instead, the mode-2 tides detected by the two moorings are northeastward waves (Figure 10e) generated by local seamounts such as Fieberling Seamount and Hoke Seamount (Kunze & Toole, 1997; Zhao, 2018), and westward waves (Figure 10f) from the continental slope, including Monterey bay (Carter, 2010). Mode-2 internal tides are more easily excited by seamounts compared to mode-1 tides due to the interplay of various factors. The generation of internal tides depends on the spectral shape of the seafloor, barotropic currents and the ocean stratification. These factors have been included in the theoretical model to calculate the global tidal energy conversion, acknowledging limitations and uncertainties (Bell, 1975; Laurent & Garrett, 2002; Nycander, 2005; Vic et al., 2019). Among these factors, the crucial role of topographic characteristics in determining dominant tidal

modes has been highlighted. For example, the modal decomposition varies between supercritical and subcritical slopes (Whalen et al., 2020). Remotely generated mode-2 tides from Hawaiian Ridge dissipate along the way and barely reach this region, that is, there is no sign of eastward waves to the moorings location. The presence of multiple sources for mode-2 tides, combined with the complex SSH field resulting from tidal interference observed in satellite observations (Figure 8b), explains the weak correlation of mode-2 tides at the two moorings (Figure 5). Furthermore, it is worth noting that the position of the two moorings in the SWOT pre-launch campaign did not align with any mode-2 tidal beam (Figure 8b), resulting in a relatively attenuated signal compared to that of mode-1 tides.

Overall, this result highlights the complexity of the internal wave field in this region and emphasizes the importance of utilizing advanced techniques, such as 2D spatial filtering and plane wave analysis, to directionally decompose and investigate individual wave characteristics. The observed diverse generation and propagation of M_2 mode-1 and mode-2 tides align with the numerical results of Zhao et al. (2019).

6. Seasonal Variations

The existence of internal tides is attributed to ocean stratification, leading to their generation and propagation being regulated by the varying ocean stratification (Munk, 1981; Wunsch, 2013). The conversion of energy from barotropic to baroclinic varies across seasons. For instance, research in the Bay of Biscay region reveals a 15% increase in conversion rate during summer (Gerkema et al., 2004). In areas like the CCS region, characterized by multiple sources, seasonal fluctuations in the conversion rates of each source result in distinct interference patterns throughout the year. As internal tides propagate, they interact with seasonally varying mesoscale currents and eddies, which affect their amplitude and phase speed through refraction and scattering (Duda et al., 2018; Ponte & Klein, 2015). Furthermore, seasonal changes in stratification, influenced by solar radiation and wind-driven circulation, also impact the propagation of internal tides (Buijsman et al., 2017; Müller et al., 2012). In the CCS region, previous study has found that the generation and propagation of internal tides are influenced by seasonal changes in stratification, background currents, and eddies (Johnston & Rudnick, 2015; Zhao et al., 2012). In winter with weak stratification, tides propagate more slowly (Zhao, 2021). This weakened stratification is likely due to the cooling of the surface waters and weaker alongshore winds south of Cape Mendocino, which result in less restratification (Checkley & Barth, 2009). The propagation speed of tidal waves during different seasons provides valuable information about ocean stratification and heat distribution.

To address this, we utilize the latest seasonal altimetry model (Section 3) to investigate the seasonal variations of mode-1 M_2 internal tides. The same mapping procedure employed in the 27-year-coherent model is used, but with four seasonal subsets. We decompose the waves into three propagation directions, maintaining the same range as in the 27-year-coherent model for comparison. Different seasonal models are analyzed by looking at the SSHAs and the magnitude and direction of energy flux in the CCS region.

6.1. Interference Patterns

The mode-1 internal tidal field associated with SSHAs exhibits a complex pattern in all of the seasonal models (see Figure S8 in Supporting Information S1). The averaged Pearson correlation coefficient of SSHA between every two seasonal models is 0.84, indicating the statistical importance of the seasonality on the internal tidal field. For the SWOT mission (swaths in green in Figure S8 in Supporting Information S1), it serves as a compelling example of why it is crucial to account for the complexity and seasonality of internal tides when applying tidal correction. Due to the complex multi-wave interference, it is challenging to quantitatively analyze the seasonality in this region. Therefore, we employ multi-wave decomposition techniques for each seasonal model.

6.2. Generation Sites

We decompose the waves from all four seasonal models into three propagation directions and examine the energy flux (W/m) in each direction (Figure 11). To quantify the seasonal effects on the generation and propagation of mode-1 tides, for each direction, we analyze data along two cross sections roughly perpendicular to the propagation shown by the striped lines.

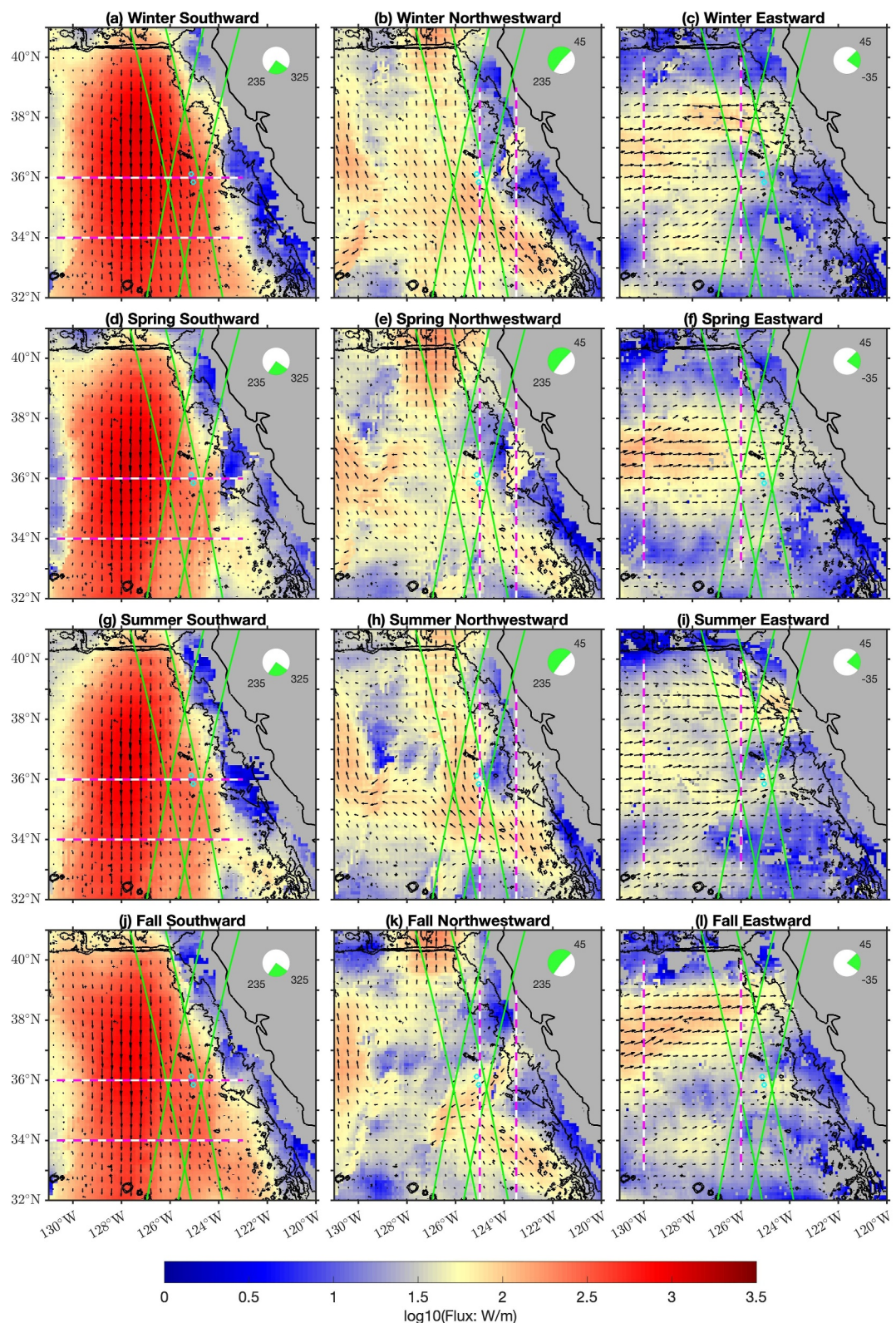


Figure 11.

The southward waves (Figures 11a, 11d, 11g, and 11j) originating from the Mendocino Ridge play a consistently dominant role throughout the year. We focus on two zonal cross sections at 34°N and 36°N (striped lines). The 36°N section represents the energy peak of the southward waves, while the 34°N section represents the energy dissipation during propagation. For each section, we integrate the energy flux between 123°W and 131°W. The result will be discussed in the following section.

For the northwestward waves (Figures 11b, 11e, 11h, and 11k), we focus on the seasonal variations of the tidal beam from the SCB and the tidal beam from the 36.5–37.5°N continental slope (hereinafter as “36.5–37.5°N”) in each seasonal model. The complex topography of islands, ridges, sills, deep basins, headlands, bays, and shelves in the SCB leads to an active internal wave field (Buijsman et al., 2012; Lerczak et al., 2003). The tidal beams from two sources are consistent with the numerical results of Zhao et al. (2019) (see Figure 8 in Zhao et al. (2019)). We select two meridional sections at 123.5°W and 125°W (striped lines) and integrate the energy flux between 32°N and 39°N. The two sections are chosen at the location before (123.5°W) and after (125°W) the waves from two sources merge. More quantitative analysis of the relative strengths of the two sources and their seasonality will be discussed in the next section.

The eastward waves (Figures 11c, 11f, 11i, and 11l), mainly generated from the Hawaiian Ridge, are evident in spring and fall. We quantify these seasonal variations by comparing the energy flux across two meridional sections at 126°W and 130°W (striped lines), both spanning between 33°N and 40°N. However, it is challenging to determine the main drivers of the seasonality of eastward waves. Factors such as background currents, eddies, and refraction of steep topography can alter the long-range waves generated from the Hawaiian Ridge after traveling 3,000 km (Dunphy & Lamb, 2014; Ponte & Klein, 2015). In addition, there are eastward tides possibly generated from or scattered by the local seamounts (e.g., the Spiess Seamounts Chain) and the fracture zone (e.g., the Murray Fracture Zone). This complexity of multiple sources contributes to the broad tidal beam, especially observed in the winter and summer models.

6.3. Cross Section Energy Flux

A cursory glance above indicates seasonal variations of internal tides from different directions. A more quantitative statement is obtained by looking at the energy flux through cross sections. By examining the distinct zonal (southward waves) or meridional (eastward and westward waves) variations of the cross-beam energy flux among four seasonal models and the 27-year-coherent model, we aim to gain a quantitative understanding of the magnitude and direction of energy transfer. To facilitate this analysis, we average over a box 0.5° along the section and 0.5° across the section along each of six sections (Figure 12). Moreover, we will integrate the energy along each section and compare among the seasonal models and the 27-year-coherent model.

The analysis of southward waves (Figures 12a and 12b) reveals distinct energy flux patterns along the cross sections. At both the 34°N and 36°N sections, the highest flux peaks are observed around 128°W. The spring season (blue) exhibits the strongest flux peak at the 36°N section, while the winter season (green) shows the highest flux peak at the 34°N section. In contrast, the fall season (cyan) exhibits the weakest peaks in both sections, indicating an attenuation in southward tidal wave. The width of the tidal beam is approximately 400–500 km at the 36°N section, with the widest beams observed during the winter season in both sections. Particularly between 124°W and 128°W, the flux is exceptionally elevated during the winter season. As the internal tides propagate approximately 222 km to the 34°N section, an average of 20% of their energy flux dissipates, with the spring season experiencing the highest dissipation (22.5%). Notably, at the 34°N section, all seasons experience a flux reduction around 126°W, possibly due to refraction from steep topography. The 27-year-coherent model (black) generally represents the average of the four seasonal models. The cross-beam integrated energy flux is strongest during winter (321 and 260 MW) and weakest during fall (231 and 186 MW) at both sections.

Figure 11. Fluxes of regional mode-1 M_2 internal tides from four climatological seasonal model, (a–c) winter, (d–f) spring, (g–i) summer, and (j–l) fall, all of which are shown on a logarithmic scale. The internal tidal field has been decomposed into three components by propagation direction. Directional range is shown as a green pie chart. Colors and arrows indicate the magnitude and direction of internal tides, respectively. Two cyan circles show the location of the two moorings from the Surface Water and Ocean Topography (SWOT) campaign. Green lines are the SWOT Cal/Val swath tracks. For each component, the two cross sections (striped lines) are given. The zonal cross sections are chosen at 34°N and 36°N for the southward waves. The meridional cross sections are chosen at 123.5°W and 125°W for the northwestward waves, and at 126°W and 130°W for the eastward waves.

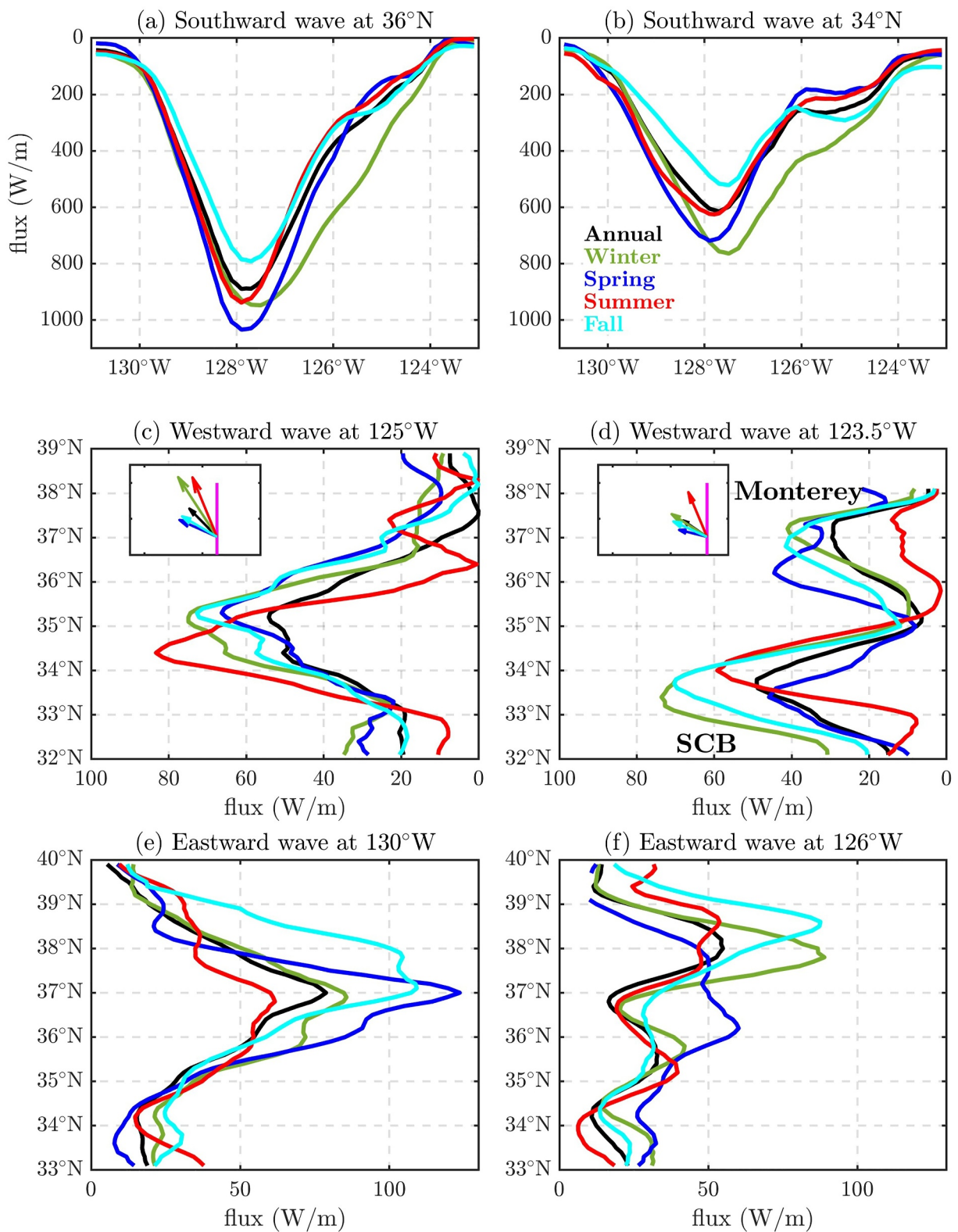


Figure 12.

For westward waves, both the relative strength of two sources (Figure 12d) and the total energy flux after their merge (Figure 12c) exhibit significant seasonal variations. At the 123.5°W section (Figure 12d), the presence of two distinct flux peaks signifies the different tidal waves originating from the SCB and the 36.5–37.5°N, consistent with Figure 11. The flux south of 35°N represents the northwestward waves from the SCB, while the flux north of 35°N represents the southwestward waves from the 36.5–37.5°N. The strength of the northwestward tides from the SCB remains relatively consistent across all seasons, except for a 40% weakening during the spring season compared to the average from the other three seasonal models. Similarly, the strength of the southwestward tides from the 36.5–37.5°N is relatively consistent across all seasons, except for a significant decrease to 25% of the average energy flux during the summer season compared to other three seasonal models. This weakening of internal tides at the 36.5–37.5°N during summer leads to a variation in the direction of the integrated energy flux in the summer model, where the flux is mainly determined by the northwestward waves from the SCB (see inset in Figure 12d). After the waves from the two sources merge at 125°W (Figure 12c), the meridional distributions of flux across different models are generally similar. However, there are some differences. In summer, the flux peak is shifted southward and observed at 34.5°N, while in the other three seasons, the peaks occur at 35.3°N. This shift is possibly due to weak generation from the 36.5–37.5°N. Additionally, during the summer season, a second peak at 37.3°N is observed, representing tides originated from the continental slope north of San Francisco Bay (e.g., Arena Canyon and Bodega Canyon). The integrated energy flux varies in magnitude and direction among the models (insets in Figures 12c and 12d), indicating significant seasonality. The phase differences among the seasonal models lead to lower tidal energy flux in the 27-year-coherent model.

Turning to eastward waves (Figures 12e and 12f), we observe flux is intensified at 130°W in both the spring and fall models (Figure 12e), consistent with the distinct tidal beam observed in Figures 11f and 11l. This energy flux is primarily generated by remotely generated waves originating from the Hawaiian Ridge. While the peaks at 37°N are higher during the spring season, the fall season exhibits the strongest integrated energy flux (41 MW), mainly attributed to the relatively strong tidal flux between 37.5°N and 39°N. At the 126°W section, the flux peak is around 38°N. Particularly during the fall and winter seasons, the flux peaks are twice as strong as those from the 27-year-coherent and other seasonal models. Dissipation occurs in all seasons after tides propagate to 126°W. However, the energy flux redistribution observed in summer and the formation of the winter peak after propagating 400 km indicate the influence of local generation from nearby seamounts and refraction of the fracture zone. These factors contribute to the complexity of the eastward tidal wave dynamics in the region.

To summarize, southward waves from the Mendocino Ridge consistently play a dominant role throughout the year, with maximum amplitude in winter and the minimum in fall. However, during fall and spring, we observe the strongest eastward waves, generated remotely from the Hawaiian Ridge. Westward waves from the 36.5–37.5°N continental slope are weakest during summer while those from the SCB are weakest during spring. To quantify the seasonal variability for waves from each direction, we calculate the coefficient of variation of integrated energy flux in four seasons. The westward waves have the highest variability of flux with $\pm 22\%$, while the southward waves have the lowest variability with $\pm 13\%$.

As a simplified representation of the complex internal tidal field, this cross-section analysis could potentially underestimate the magnitude of the energy flux, as it only accounts for the portion that is orthogonal to the section. Also, the seasonal variations may be dependent on the definition of four seasons and corresponding ocean conditions. The definition of seasons and corresponding ocean conditions can vary depending on the research and the specific region of study. For the CCS region, some studies have utilized the alongshore wind direction as a criterion for defining seasons. In this approach, upwelling-favorable conditions are characterized by equatorward winds, while poleward winds and storms indicate downwelling-favorable conditions (Checkley & Barth, 2009; Dettinger, 2011). This leads to a longer summer (June–September) and winter (December–February). Other

Figure 12. Seasonality of cross-beam energy flux from three directions. Southward energy flux is illustrated across (a) 36°N and (b) 34°N. Note that the flux is shown in the reversed direction of the y axis to align with southward waves. At both latitudes, each section spans between 123°W and 131°W. Westward energy flux is presented across (c) 125°W and (d) 123.5°W. Note that the flux is shown in the reversed direction of the x axis to align with westward waves. Each section spans between 32°N and 39°N. The cross-section summation of energy flux for five models is shown as vectors in the inset at the upper left corner. Eastward energy flux is showcased across (e) 130°W and (f) 126°W. Each section spans between 33°N and 40°N. The 27-year-coherent model is in black and the four seasonal models are in green for winter, blue for spring, red for summer, and cyan for fall.

factors, such as water temperature, energy sink from wind-current feedback (Delpech et al., 2023), and local atmospheric conditions, can also influence the seasonal variability of internal tides.

The seasonal variations identified through altimetry have limitations in fully elucidating the underlying physics, as altimetry solely provides data on SSH and lacks information about what lies beneath the surface. Moving forward, we are eager to collaborate with modelers to gain a deeper understanding of the mechanisms driving the seasonal variations. Despite these considerations, the evident seasonality of internal tides in the region has significant implications for ocean mixing and circulation. For example, the inclusion of seasonal variability in ocean models is crucial for capturing the dynamic nature of internal tides, leading to improved model predictions and understanding of multiscale oceanic phenomena.

7. Conclusions and Discussion

The study examines the temporal and spatial variations of semidiurnal internal tides off central California. This is achieved by utilizing both moored data from the SWOT pre-launch campaign in 2019 and internal tidal models from 27 years of altimetry. Pronounced semidiurnal internal tides are observed at both moorings. The south mooring exhibits stronger semidiurnal tidal energy, while the north mooring shows higher amplitudes of the mode-1 M_2 internal tide. It is plausible that the warm anticyclone eddy during the measurements partially leads to the temporal variations by slowing down the southward mode-1 M_2 tides.

The satellite altimetry models help explain the spatial variations of M_2 tides observed by the moorings and showcase the mean and seasonal variability of mode-1 and mode-2 tides in the region. Different characteristics are observed between mode-1 and mode-2 M_2 tides, indicating distinct generation sources. Mode-1 tides are primarily generated from the Mendocino Ridge and the 36.5–37.5°N California continental slope, while mode-2 tides originate mostly from local seamounts and Monterey Bay. Additionally, seasonal variations are observed in the generation and propagation of the regional mode-1 M_2 internal tides. The winter season exhibits the strongest southward waves from the Mendocino Ridge and westward waves from the continental slope. In contrast, the fall season shows the strongest eastward waves, generated remotely from the Hawaiian Ridge, while exhibiting the weakest southward waves. Westward waves are weakest during the summer, possibly due to weak generation from the continental slope, increased dissipation during propagation, or a combination of both factors. Overall, the westward waves have the highest seasonal variability of tidal flux with $\pm 22\%$, while the southward waves have the lowest variability with $\pm 13\%$.

This analysis has limitations. The moorings have finite vertical resolution which limits the ability to accurately resolve the high modes (Nash et al., 2005). The analysis finds relatively weak internal tides compared to other regions such as the Hawaiian Ridge, the South China Sea, the Tasman Sea and the Mid-Atlantic Ridge (Alford et al., 2015; Xu et al., 2016; Zhao et al., 2016) which may introduce uncertainties due to the lower signal to noise. This is partially addressed by a sensitivity analysis of the mode fitting number and the displacement correction for the mooring motion (see Supporting Information S1). It is challenging to estimate the impact of mesoscale eddies on internal tides solely through short-term two-mooring measurements. The result is only suggestive, but offers some insights; an array of moorings with a longer measurement period would be better (Huang et al., 2018). Further investigation with numerical simulations is required to unveil the mechanism of the seasonality of internal tides that we discuss above, recognizing that the altimetry data only contain the ocean surface information. Such a simulation would need to include an accurate seasonal cycle of the upper ocean and accurate representation of internal tidal interactions with other internal waves, background geostrophic currents, and bottom topography, as well as the effects of these interactions on the tidal dissipation.

This study enhances our understanding of internal tide variability within the CCS region, providing valuable insights for future research for SWOT (Fu et al., 2024; Qiu et al., 2024) and numerical modeling endeavors (Arbic, 2022). For the SWOT tidal aliasing issue due to its long repeat cycle, it is crucial to correct for unresolved internal tides before deriving and analyzing submesoscale dynamics from the SWOT data, especially in regions where significant mode-1 and mode-2 baroclinic tides exist (Carrere et al., 2021; Chavanne & Klein, 2010; Qiu et al., 2018). Our findings suggest that the incorporation of seasonal variability of internal tides holds significant potential to improve the SWOT tidal correction.

Data Availability Statement

The SWOT pre-launch field campaign 2019–2020 data were downloaded from the NASA Physical Oceanography Distributed Active Archive Center (SWOT, 2022a, 2022b, 2022c). The MODIS Aqua Level 3 sea surface temperature product was downloaded from NASA Physical Oceanography Distributed Active Archive Center (NASA/JPL, 2020). The World Ocean Atlas 2018 is produced and made available by the NOAA National Centers for Environmental Information (Boyer et al., 2019). The absolute dynamic topography and the surface geostrophic velocity anomaly data are collected from the Copernicus Marine Service (European Union-Copernicus Marine Service, 2021). The bathymetry information is referred to in the General Bathymetric Chart of the Oceans (GEBCO Compilation Group, 2023). The satellite altimetry internal tide models are accessible to the public (Zhao, 2024).

Acknowledgments

This work was supported by NSF projects OCE1947592, OCE2149028 and 80NNSC19K1007 P0007. The research was carried out at the Jet Propulsion Laboratory, California Institute of Technology, under a contract with the National Aeronautics and Space Administration (80NM0018D0004). We acknowledge the efforts of those involved in and supporting the public availability of the SWOT pre-launch campaign mooring data and the satellite altimeter data used here. We express gratitude to the anonymous reviewers for their valuable suggestions and comments.

References

Alford, M. H. (2010). Sustained, full-water-column observations of internal waves and mixing near Mendocino escarpment. *Journal of Physical Oceanography*, 40(12), 2643–2660. <https://doi.org/10.1175/2010JPO4502.1>

Alford, M. H., Mickett, J. B., Zhang, S., MacCready, P., Zhao, Z., & Newton, J. (2012). Internal waves on the Washington Continental Shelf. *Oceanography*, 25(2), 66–79. <https://doi.org/10.5670/oceanog.2012.43>

Alford, M. H., Peacock, T., MacKinnon, J. A., Nash, J. D., Buijsman, M. C., Centurioni, L. R., et al. (2015). The formation and fate of internal waves in the South China Sea. *Nature*, 521(7550), 65–69. <https://doi.org/10.1038/nature14399>

Althaus, A. M., Kunze, E., & Sanford, T. B. (2003). Internal tide radiation from Mendocino escarpment. *Journal of Physical Oceanography*, 33(7), 1510–1527. [https://doi.org/10.1175/1520-0485\(2003\)033\(1510:ITRFME\)2.0.CO;2](https://doi.org/10.1175/1520-0485(2003)033(1510:ITRFME)2.0.CO;2)

Ansong, J. K., Arbic, B. K., Alford, M. H., Buijsman, M. C., Shriner, J. F., Zhao, Z., et al. (2017). Semidiurnal internal tide energy fluxes and their variability in a Global Ocean Model and moored observations. *Journal of Geophysical Research: Oceans*, 122(3), 1882–1900. <https://doi.org/10.1002/2016JC012184>

Arbic, B. K. (2022). Incorporating tides and internal gravity waves within global ocean general circulation models: A review. *Progress in Oceanography*, 206, 102824. <https://doi.org/10.1016/j.pocean.2022.102824>

Bell, T. H. (1975). Lee waves in stratified flows with simple harmonic time dependence. *Journal of Fluid Mechanics*, 76(4), 705–722. <https://doi.org/10.1017/S0022112075000560>

Boyer, T. P., García, H. E., Locarnini, R. A., Zweng, M. M., Mishonov, A. V., Reagan, J. R., et al. (2019). World Ocean Atlas 2018 [Dataset]. Retrieved from <https://www.ncei.noaa.gov/archive/accession/NCEI-WOA18>

Brink, K. H. (1995). Tidal and lower frequency currents above Fieberling Guyot. *Journal of Geophysical Research*, 100(C6), 10817–10832. <https://doi.org/10.1029/95JC00998>

Buijsman, M. C., Arbic, B. K., Richman, J. G., Shriner, J. F., Wallcraft, A. J., & Zamudio, L. (2017). Semidiurnal internal tide incoherence in the equatorial Pacific. *Journal of Geophysical Research: Oceans*, 122(7), 5286–5305. <https://doi.org/10.1002/2016JC012590>

Buijsman, M. C., Uchiyama, Y., McWilliams, J. C., & Hill-Lindsay, C. R. (2012). Modeling semidiurnal internal tide variability in the Southern California Bight. *Journal of Physical Oceanography*, 42(1), 62–77. <https://doi.org/10.1175/2011JPO4597.1>

Carrere, L., Arbic, B. K., Dushaw, B., Egbert, G., Erofeeva, S., Lyard, F., et al. (2021). Accuracy assessment of global internal-tide models using satellite altimetry. *Ocean Science*, 17(1), 147–180. <https://doi.org/10.5194/os-17-147-2021>

Carter, G. S. (2010). Barotropic and baroclinic M_2 tides in the Monterey Bay Region. *Journal of Physical Oceanography*, 40(8), 1766–1783. <https://doi.org/10.1175/2010JPO4274.1>

Carter, G. S., Gregg, M. C., & Lien, R.-C. (2005). Internal waves, solitary-like waves, and mixing on the Monterey Bay shelf. *Continental Shelf Research*, 25(12), 1499–1520. <https://doi.org/10.1016/j.csr.2005.04.011>

Chavanne, C. P., & Klein, P. (2010). Can oceanic submesoscale processes be observed with satellite altimetry? *Geophysical Research Letters*, 37(22), L22602. <https://doi.org/10.1029/2010GL045057>

Checkley, D. M., & Barth, J. A. (2009). Patterns and processes in the California Current System. *Progress in Oceanography*, 83(1), 49–64. <https://doi.org/10.1016/j.pocean.2009.07.028>

de Lavergne, C., Falahat, S., Madec, G., Roquet, F., Nylander, J., & Vic, C. (2019). Toward global maps of internal tide energy sinks. *Ocean Modelling*, 137, 52–75. <https://doi.org/10.1016/j.ocemod.2019.03.010>

Delpech, A., Barkan, R., Renault, L., McWilliams, J., Siyanbola, O. Q., Buijsman, M. C., & Arbic, B. K. (2023). Wind-current feedback is an energy sink for oceanic internal waves. *Scientific Reports*, 13(1), 5915. <https://doi.org/10.1038/s41598-023-32909-6>

Dettinger, M. (2011). Climate change, atmospheric rivers, and floods in California – A multimodel analysis of storm frequency and magnitude changes I. *JAWRA Journal of the American Water Resources Association*, 47(3), 514–523. <https://doi.org/10.1111/j.1752-1688.2011.00546.x>

Duda, T. F., Lin, Y.-T., Buijsman, M., & Newhall, A. E. (2018). Internal tidal modal ray refraction and energy ducting in baroclinic Gulf Stream Currents. *Journal of Physical Oceanography*, 48(9), 1969–1993. <https://doi.org/10.1175/JPO-D-18-0031.1>

Dunphy, M., & Lamb, K. G. (2014). Focusing and vertical mode scattering of the first mode internal tide by mesoscale eddy interaction. *Journal of Geophysical Research: Oceans*, 119(1), 523–536. <https://doi.org/10.1002/2013JC009293>

Dunphy, M., Ponte, A. L., Klein, P., & Gentil, S. L. (2017). Low-mode internal tide propagation in a turbulent eddy field. *Journal of Physical Oceanography*, 47(3), 649–665. <https://doi.org/10.1175/JPO-D-16-0099.1>

European Union-Copernicus Marine Service. (2021). Global ocean gridded 14 sea surface heights and derived variables reprocessed (1993–ongoing) [Dataset]. <https://doi.org/10.48670/moi-00148>

Fu, L. L., Pavelsky, T., Cretaux, J. F., Morrow, R., Farrar, J. T., Vaze, P., et al. (2024). The surface water and ocean topography mission: A breakthrough in radar remote sensing of the ocean and land surface water. *Geophysical Research Letters*, 51(4), e2023GL107652. <https://doi.org/10.1029/2023GL107652>

GEBCO Compilation Group. (2023). Gebco 2023 grid [Dataset]. <https://doi.org/10.5285/f98b053b-0cbc-6e23-e053-6e86abc0af7b>

Gerkema, T., Lam, F. A., & Maas, L. R. M. (2004). Internal tides in the Bay of Biscay: Conversion rates and seasonal effects. *Deep Sea Research Part II: Topical Studies in Oceanography*, 51(25–26), 2995–3008. <https://doi.org/10.1016/j.dsrr.2004.09.012>

Gill, A. E. (1982). *Atmosphere-ocean dynamics* (Vol. 30). Academic Press.

Haney, R. L., Hale, R. A., & Dietrich, D. E. (2001). Offshore propagation of eddy kinetic energy in the California Current. *Journal of Geophysical Research*, 106(C6), 11709–11717. <https://doi.org/10.1029/2000JC000433>

Huang, X., Wang, Z., Zhang, Z., Yang, Y., Zhou, C., Yang, Q., et al. (2018). Role of mesoscale eddies in modulating the semidiurnal internal tide: Observation results in the Northern South China Sea. *Journal of Physical Oceanography*, 48(8), 1749–1770. <https://doi.org/10.1175/JPO-D-17-0209.1>

Johnston, T. M. S., & Rudnick, D. L. (2015). Trapped diurnal internal tides, propagating semidiurnal internal tides, and mixing estimates in the California Current System from sustained glider observations, 2006–2012. *Deep Sea Research Part II: Topical Studies in Oceanography*, 112, 61–78. <https://doi.org/10.1016/j.dsr2.2014.03.009>

Kelly, S. M., Jones, N. L., Nash, J. D., & Waterhouse, A. F. (2013). The geography of semidiurnal mode-1 internal-tide energy loss. *Geophysical Research Letters*, 40(17), 4689–4693. <https://doi.org/10.1002/grl.50872>

Kelly, S. M., Lermusiaux, P. F. J., Duda, T. F., & Haley, P. J. (2016). A coupled-mode shallow-water model for tidal analysis: Internal tide reflection and refraction by the Gulf Stream. *Journal of Physical Oceanography*, 46(12), 3661–3679. <https://doi.org/10.1175/JPO-D-16-0018.1>

Köhler, J., Walter, M., Mertens, C., Stiehler, J., Li, Z., Zhao, Z., et al. (2019). Energy flux observations in an internal tide beam in the Eastern North Atlantic. *Journal of Geophysical Research: Oceans*, 124(8), 5747–5764. <https://doi.org/10.1029/2019JC015156>

Kunze, E., & Toole, J. M. (1997). Tidally driven vorticity, diurnal shear, and turbulence atop Fieberling Seamount. *Journal of Physical Oceanography*, 27(12), 2663–2693. [https://doi.org/10.1175/1520-0485\(1997\)027<2663:tdvds>2.0.co;2](https://doi.org/10.1175/1520-0485(1997)027<2663:tdvds>2.0.co;2)

Kurian, J., Colas, F., Capet, X., McWilliams, J. C., & Chelton, D. B. (2011). Eddy properties in the California Current System. *Journal of Geophysical Research*, 116(C8), C08027. <https://doi.org/10.1029/2010JC006895>

Laurent, L. S., & Garrett, C. (2002). The role of internal tides in mixing the deep ocean. *Journal of Physical Oceanography*, 32(10), 2882–2899. [https://doi.org/10.1175/1520-0485\(2002\)032\(2882:TROITI\)2.0.CO;2](https://doi.org/10.1175/1520-0485(2002)032(2882:TROITI)2.0.CO;2)

Lerczak, J. A., Winant, C. D., & Hendershott, M. C. (2003). Observations of the semidiurnal internal tide on the southern California slope and shelf. *Journal of Geophysical Research*, 108(C3), 3068. <https://doi.org/10.1029/2001JC001128>

Löb, J., Köhler, J., Mertens, C., Walter, M., Li, Z., von Storch, J.-S., et al. (2020). Observations of the low-mode internal tide and its interaction with mesoscale flow South of the Azores. *Journal of Geophysical Research: Oceans*, 125(11), e2019JC015879. <https://doi.org/10.1029/2019JC015879>

Mazloff, M. R., Cornuelle, B., Gille, S. T., & Wang, J. (2020). The importance of remote forcing for regional modeling of internal waves. *Journal of Geophysical Research: Oceans*, 125(2), e2019JC015623. <https://doi.org/10.1029/2019JC015623>

McDougall, T. J., & Barker, P. M. (2011). Getting started with TEOS-10 and the Gibbs Seawater (GSW) oceanographic toolbox. *SCOR/IAPSO WG*, 127(532), 1–28.

Melet, A. V., Hallberg, R., & Marshall, D. P. (2022). Chapter 2 - The role of ocean mixing in the climate system. In *Ocean mixing* (pp. 5–34). Elsevier. <https://doi.org/10.1016/B978-0-12-821512-8.00009-8>

Müller, M., Cherniawsky, J. Y., Foreman, M. G. G., & von Storch, J.-S. (2012). Global M_2 internal tide and its seasonal variability from high resolution ocean circulation and tide modeling. *Geophysical Research Letters*, 39(19), L19607. <https://doi.org/10.1029/2012GL053320>

Munk, W. H. (1981). Internal waves and small-scale processes. In *Evolution of physical oceanography*.

Musgrave, R. C., MacKinnon, J. A., Pinkel, R., Waterhouse, A. F., Nash, J., & Kelly, S. M. (2017). The influence of subinertial internal tides on near-topographic turbulence at the Mendocino Ridge: Observations and modeling. *Journal of Physical Oceanography*, 47(8), 2139–2154. <https://doi.org/10.1175/JPO-D-16-0278.1>

NASA/JPL. (2020). MODIS aqua level 3 SST mid-IR daily 4km nighttime v2019.0 [Dataset]. <https://doi.org/10.5067/MODAM-1D4N9>

Nash, J. D., Alford, M. H., & Kunze, E. (2005). Estimating internal wave energy fluxes in the ocean. *Journal of Atmospheric and Oceanic Technology*, 22(10), 1551–1570. <https://doi.org/10.1175/JTECH1784.1>

Nelson, A. D., Arbic, B. K., Zaron, E. D., Savage, A. C., Richman, J. G., Buijsman, M. C., & Shriver, J. F. (2019). Toward realistic nonstationarity of semidiurnal baroclinic tides in a hydrodynamic model. *Journal of Geophysical Research: Oceans*, 124(9), 6632–6642. <https://doi.org/10.1029/2018JC014737>

Nycander, J. (2005). Generation of internal waves in the deep ocean by tides. *Journal of Geophysical Research*, 110(C10), C10028. <https://doi.org/10.1029/2004JC002487>

Olbers, D. J. (1983). Models of the oceanic internal wave field. *Reviews of Geophysics*, 21(7), 1567–1606. <https://doi.org/10.1029/RG021i007p01567>

Onuki, Y., & Hibiya, T. (2018). Decay rates of internal tides estimated by an improved wave–wave interaction analysis. *Journal of Physical Oceanography*, 48(11), 2689–2701. <https://doi.org/10.1175/JPO-D-17-0278.1>

Pawlowicz, R., Beardsley, B., & Lentz, S. (2002). Classical tidal harmonic analysis including error estimates in MATLAB using T_tide. *Computers & Geosciences*, 28(8), 929–937. [https://doi.org/10.1016/S0098-3004\(02\)00013-4](https://doi.org/10.1016/S0098-3004(02)00013-4)

Polzin, K. L. (2008). Mesoscale eddy–internal wave coupling. Part I: Symmetry, wave capture, and results from the mid-ocean dynamics experiment. *Journal of Physical Oceanography*, 38(11), 2556–2574. <https://doi.org/10.1175/2008JPO3666.1>

Ponte, A. L., & Klein, P. (2015). Incoherent signature of internal tides on sea level in idealized numerical simulations. *Geophysical Research Letters*, 42(5), 1520–1526. <https://doi.org/10.1002/2014GL062583>

Qiu, B., Chen, S., Klein, P., Sasaki, H., & Sasaki, Y. (2014). Seasonal mesoscale and submesoscale eddy variability along the North Pacific subtropical countercurrent. *Journal of Physical Oceanography*, 44(12), 3079–3098. <https://doi.org/10.1175/JPO-D-14-0071.1>

Qiu, B., Chen, S., Klein, P., Wang, J., Torres, H., Fu, L.-L., & Menemenlis, D. (2018). Seasonality in transition scale from balanced to unbalanced motions in the world ocean. *Journal of Physical Oceanography*, 48(3), 591–605. <https://doi.org/10.1175/JPO-D-17-0169.1>

Qiu, B., Chen, S., Wang, J., & Fu, L. L. (2024). Seasonal and fortnight variations in internal solitary waves in the Indonesian seas from the SWOT measurements. *Journal of Geophysical Research: Oceans*, 129(7), e2024JC021086. <https://doi.org/10.1029/2024JC021086>

Rainville, L., Johnston, T. M. S., Carter, G. S., Merrifield, M. A., Pinkel, R., Worcester, P. F., & Dushaw, B. D. (2010). Interference pattern and propagation of the M_2 internal tide south of the Hawaiian Ridge. *Journal of Physical Oceanography*, 40(2), 311–325. <https://doi.org/10.1175/2009JPO4256.1>

Rainville, L., & Pinkel, R. (2006). Propagation of low-mode internal waves through the ocean. *Journal of Physical Oceanography*, 36(6), 1220–1236. <https://doi.org/10.1175/JPO2889.1>

Ray, R. D., & Zaron, E. D. (2016). M_2 internal tides and their observed wavenumber spectra from satellite altimetry. *Journal of Physical Oceanography*, 46(1), 3–22. <https://doi.org/10.1175/JPO-D-15-0065.1>

Rudnick, D. L., Zaba, K. D., Todd, R. E., & Davis, R. E. (2017). A climatology of the California Current System from a network of underwater gliders. *Progress in Oceanography*, 154, 64–106. <https://doi.org/10.1016/j.pocean.2017.03.002>

Sasaki, H., Klein, P., Qiu, B., & Sasai, Y. (2014). Impact of oceanic-scale interactions on the seasonal modulation of ocean dynamics by the atmosphere. *Nature Communications*, 5(1), 5636. <https://doi.org/10.1038/ncomms6636>

Savage, A. C., Waterhouse, A. F., & Kelly, S. M. (2020). Internal tide nonstationarity and wave–mesoscale interactions in the Tasman Sea. *Journal of Physical Oceanography*, 50(10), 2931–2951. <https://doi.org/10.1175/JPO-D-19-0283.1>

Shakespeare, C. J. (2023). Eddy acceleration and decay driven by internal tides. *Journal of Physical Oceanography*, 53(12), 2787–2796. <https://doi.org/10.1175/JPO-D-23-0127.1>

Sharples, J., Tweddle, J. F., Mattias Green, J. A., Palmer, M. R., Kim, Y.-N., Hickman, A. E., et al. (2007). Spring–neap modulation of internal tide mixing and vertical nitrate fluxes at a shelf edge in summer. *Limnology and Oceanography*, 52(5), 1735–1747. <https://doi.org/10.4319/lo.2007.52.5.1735>

Shriver, J. F., Richman, J. G., & Arbic, B. K. (2014). How stationary are the internal tides in a high-resolution global ocean circulation model? *Journal of Geophysical Research: Oceans*, 119(5), 2769–2787. <https://doi.org/10.1002/2013JC009423>

SWOT. (2022a). SWOT 2019–2020 prelaunch oceanography field campaign SIO moored fixed-depth CTDs [Dataset]. <https://doi.org/10.5067/SWTPR-CTD01>

SWOT. (2022b). SWOT 2019–2020 prelaunch oceanography field campaign SIO mooring WireWalker (WW) [Dataset]. <https://doi.org/10.5067/SWTPR-WW001>

SWOT. (2022c). SWOT 2019–2020 prelaunch oceanography field campaign WHOI/NOAA moored Fixed-Depth CTDs [Dataset]. <https://doi.org/10.5067/SWTPR-CTD11>

Terker, S. R., Girton, J. B., Kunze, E., Klymak, J. M., & Pinkel, R. (2014). Observations of the internal tide on the California continental margin near Monterey Bay. *Continental Shelf Research*, 82, 60–71. <https://doi.org/10.1016/j.csr.2014.01.017>

Thomson, D. (1982). Spectrum estimation and harmonic analysis. *Proceedings of the IEEE*, 70(9), 1055–1096. <https://doi.org/10.1109/PROC.1982.12433>

Torgrimson, G. M., & Hickey, B. M. (1979). Barotropic and baroclinic tides over the continental slope and shelf off Oregon. *Journal of Physical Oceanography*, 9(5), 945–961. [https://doi.org/10.1175/1520-0485\(1979\)009\(0945:BABTOT\)2.0.CO;2](https://doi.org/10.1175/1520-0485(1979)009(0945:BABTOT)2.0.CO;2)

Vic, C., Naveira Garabato, A. C., Green, J. A. M., Waterhouse, A. F., Zhao, Z., Melet, A., et al. (2019). Deep-ocean mixing driven by small-scale internal tides. *Nature Communications*, 10(1), 2099. <https://doi.org/10.1038/s41467-019-10149-5>

Wang, J., Fu, L.-L., Haines, B., Lankhorst, M., Lucas, A. J., Farrar, J. T., et al. (2022). On the development of SWOT in situ calibration/validation for short-wavelength ocean topography. *Journal of Atmospheric and Oceanic Technology*, 39(5), 595–617. <https://doi.org/10.1175/JTECH-D-21-0039.1>

Whalen, C. B., de Lavergne, C., Naveira Garabato, A. C., Klymak, J. M., MacKinnon, J. A., & Sheen, K. L. (2020). Internal wave-driven mixing: Governing processes and consequences for climate. *Nature Reviews Earth & Environment*, 1(11), 606–621. <https://doi.org/10.1038/s43017-020-0097-z>

Wunsch, C. (1975). Internal tides in the ocean. *Reviews of Geophysics*, 13(1), 167–182. <https://doi.org/10.1029/RG013i001p00167>

Wunsch, C. (2013). Baroclinic motions and energetics as measured by altimeters. *Journal of Atmospheric and Oceanic Technology*, 30(1), 140–150. <https://doi.org/10.1175/JTECH-D-12-00035.1>

Xu, Z., Liu, K., Yin, B., Zhao, Z., Wang, Y., & Li, Q. (2016). Long-range propagation and associated variability of internal tides in the South China Sea. *Journal of Geophysical Research: Oceans*, 121(11), 8268–8286. <https://doi.org/10.1002/2016JC012105>

Zaron, E. D., & Egbert, G. D. (2014). Time-variable refraction of the internal tide at the Hawaiian Ridge. *Journal of Physical Oceanography*, 44(2), 538–557. <https://doi.org/10.1175/JPO-D-12-0238.1>

Zaron, E. D., & Ray, R. D. (2017). Using an altimeter-derived internal tide model to remove tides from in situ data. *Geophysical Research Letters*, 44(9), 4241–4245. <https://doi.org/10.1002/2017GL072950>

Zhao, Z. (2016). Using CryoSat-2 altimeter data to evaluate M_2 internal tides observed from multisatellite altimetry. *Journal of Geophysical Research: Oceans*, 121(7), 5164–5180. <https://doi.org/10.1002/2016JC011805>

Zhao, Z. (2018). The global mode-2 M_2 internal tide. *Journal of Geophysical Research: Oceans*, 123(11), 7725–7746. <https://doi.org/10.1029/2018JC014475>

Zhao, Z. (2019). Mapping internal tides from satellite altimetry without blind directions. *Journal of Geophysical Research: Oceans*, 124(12), 8605–8625. <https://doi.org/10.1029/2019JC015507>

Zhao, Z. (2021). Seasonal mode-1 M_2 internal tides from satellite altimetry. *Journal of Physical Oceanography*, 51(9), 3015–3035. <https://doi.org/10.1175/JPO-D-21-0001.1>

Zhao, Z. (2022). Development of the yearly mode-1 M_2 internal tide model in 2019. *Journal of Atmospheric and Oceanic Technology*, 39(4), 463–478. <https://doi.org/10.1175/JTECH-D-21-0116.1>

Zhao, Z. (2024). Internal tides off California observed by satellite altimetry [Dataset]. <https://doi.org/10.6084/m9.figshare.24939270.v1>

Zhao, Z., Alford, M. H., Girton, J. B., Rainville, L., & Simmons, H. L. (2016). Global observations of open-ocean mode-1 M_2 internal tides. *Journal of Physical Oceanography*, 46(6), 1657–1684. <https://doi.org/10.1175/JPO-D-15-0105.1>

Zhao, Z., Alford, M. H., Lien, R.-C., Gregg, M. C., & Carter, G. S. (2012). Internal tides and mixing in a submarine canyon with time-varying stratification. *Journal of Physical Oceanography*, 42(12), 2121–2142. <https://doi.org/10.1175/JPO-D-12-045.1>

Zhao, Z., Alford, M. H., MacKinnon, J. A., & Pinkel, R. (2010). Long-range propagation of the semidiurnal internal tide from the Hawaiian Ridge. *Journal of Physical Oceanography*, 40(4), 713–736. <https://doi.org/10.1175/2009PO4207.1>

Zhao, Z., & Qiu, B. (2023). Seasonal west-east seesaw of M_2 internal tides from the Luzon Strait. *Journal of Geophysical Research: Oceans*, 128(3), e2022JC019281. <https://doi.org/10.1029/2022JC019281>

Zhao, Z., Wang, J., Menemenlis, D., Fu, L.-L., Chen, S., & Qiu, B. (2019). Decomposition of the multimodal multidirectional M_2 internal tide field. *Journal of Atmospheric and Oceanic Technology*, 36(6), 1157–1173. <https://doi.org/10.1175/JTECH-D-19-0022.1>

Zilberman, N. V., Merrifield, M. A., Carter, G. S., Luther, D. S., Levine, M. D., & Boyd, T. J. (2011). Incoherent nature of M_2 internal tides at the Hawaiian Ridge. *Journal of Physical Oceanography*, 41(11), 2021–2036. <https://doi.org/10.1175/JPO-D-10-05009.1>

References From the Supporting Information

de Boyer Montégut, C., Madec, G., Fischer, A. S., Lazar, A., & Jidicoune, D. (2004). Mixed layer depth over the global ocean: An examination of profile data and a profile-based climatology. *Journal of Geophysical Research*, 109(C12), C12003. <https://doi.org/10.1029/2004JC002378>

Garrett, C. (2003). Internal tides and ocean mixing. *Science*, 301(5641), 1858–1859. <https://doi.org/10.1126/science.1090002>

Kerry, C. G., Powell, B. S., & Carter, G. S. (2016). Quantifying the incoherent M_2 internal tide in the Philippine Sea. *Journal of Physical Oceanography*, 46(8), 2483–2491. <https://doi.org/10.1175/JPO-D-16-0023.1>

Kunze, E. (2017). Internal-wave-driven mixing: Global geography and budgets. *Journal of Physical Oceanography*, 47(6), 1325–1345. <https://doi.org/10.1175/JPO-D-16-0141.1>

Li, Q., & Fox-Kemper, B. (2017). Assessing the effects of Langmuir turbulence on the entrainment buoyancy flux in the ocean surface boundary layer. *Journal of Physical Oceanography*, 47(12), 2863–2886. <https://doi.org/10.1175/JPO-D-17-0085.1>

Wunsch, C., & Ferrari, R. (2004). Vertical mixing, energy, and the general circulation of the oceans. *Annual Review of Fluid Mechanics*, 36(1), 281–314. <https://doi.org/10.1146/annurev.fluid.36.050802.122121>